Three-dimensional imaging and single-cell transcriptomics of the human kidney implicate perturbation of lymphatics in alloimmunity

Daniyal J Jafree[1,2], Benjamin Stewart[3,4], Maria Kolatsi-Joannou[1], Benjamin Davis[5], Hannah Mitchell[6], Lauren G Russell[1], Lucía Marinas del Rey[7,8], William J Mason[1], Byung Il Lee[9], Lauren Heptinstall[10], Gideon Pomeranz[1], Dale Moulding[1], Laura Wilson[1], Tahmina Wickenden[1], Saif Malik[1], Natalie Holroyd[11], Claire Walsh[11], Jennifer C Chandler[1], Kevin X Cao[1], Paul JD Winyard[1], Karen L Price[1], Adrian S Woolf[12,13], Marc Aurel Busche[9], Simon Walker-Samuel[11], Peter J Scambler[1], Reza Motallebzadeh[7,8], Menna R Clatworthy[3,4]*, David A Long[1]*

[1]Developmental Biology & Cancer Research & Teaching Department, UCL Great Ormond Street Institute of Child Health, UCL, London, UK; [2]UCL MB/PhD Programme, UCL, London, UK; [3]Molecular Immunity Unit, University of Cambridge, Cambridge, UK; [4]Cellular Genetics, Wellcome Sanger Institute, Hinxton UK; [5]Central Laser Facility, Science and Technologies Facilities Council, UK Research and Innovation, Didcot, Oxfordshire, UK; [6]Mathematical Sciences Research Centre, Queen's University Belfast, Belfast, UK; [7]Research Department of Surgical Biotechnology, Division of Surgery and Interventional Science, UCL, London, UK ; [8]UCL Institute of Immunity and Transplantation, UCL, London, UK; [9]UK Dementia Research Institute, UCL, London, UK; [10]UCL Department of Pathology, Royal Free Hospital, London, UK; [11]UCL Centre for Advanced Biomedical Imaging, London, UK

***: Corresponding authors**

Professor David A Long

Professor in Paediatric Nephrology & Wellcome Trust Investigator in Science,

Developmental Biology and Cancer Research & Teaching Department,

UCL Great Ormond Street Institute of Child Health,

30 Guilford Street, London, WC1N 1EH, UK

Tel.: +44(0)2079052615, Email: d.long@ucl.ac.uk

Professor Menna R Clatworthy

Molecular Immunity Unit,

University of Cambridge Department of Medicine,

MRC Laboratory of Molecular Biology,

Cambridge Biomedical Campus,

Francis Crick Avenue,

Cambridge. CB2 0QH, UK

Tel.: +44(0)1223267279, Email: mrc38@cam.ac.uk

ABSTRACT

Studies of the structural and molecular features of the lymphatic vasculature, which clears fluid, macromolecules and leukocytes from the tissue microenvironment, have largely relied on animal models, with limited information in human organs beyond traditional immunohistochemical assessment. Here, we use three-dimensional imaging and single-cell RNA-sequencing to study lymphatics in the human kidney. We found a hierarchical arrangement of lymphatic vessels within human kidneys, initiating along specialised nephron epithelium in the renal cortex and displaying a distinct, kidney-specific transcriptional profile. In chronic transplant rejection we found kidney allograft lymphatic expansion alongside a loss of structural hierarchy, with human leukocyte antigen-expressing lymphatic vessels infiltrating the medulla, presenting a putative target for alloreactive antibodies. This occurred concurrently with lymphatic vessels invading and interconnecting tertiary lymphoid structures at early stages of lymphocyte colonisation. Analysis of intercellular signalling revealed upregulation of co-inhibitory molecule-mediated $CD4^+$ T cell-lymphatic crosstalk in rejecting kidneys, potentially acting to limit local alloimmune responses. Overall, we delineate novel structural and molecular features of human kidney lymphatics and reveal perturbations to their phenotype and transcriptome in the context of alloimmunity.

SUMMARY

Lymphatics regulate fluid balance and immune cell accumulation but are under-studied in human organs such as the kidney. Jafree and colleagues profiled human kidney lymphatics using three-dimensional imaging and single-cell RNA-sequencing, revealing structural and transcriptional perturbations in rejecting kidney transplants.

INTRODUCTION

Lymphatics are blind-ended vessels that clear tissue fluid and macromolecules from the tissue microenvironment and, during inflammation, sprout to facilitate leukocyte clearance in a process termed lymphangiogenesis (Oliver et al. 2020; Petrova and Koh 2020; Stritt et al. 2021). Other lymphatic functions include absorption of dietary lipids (Bernier-Latmani and Petrova 2017), drainage of cerebrospinal fluid (Da Mesquita, Fu, et al. 2018), cholesterol transport (Ouimet et al. 2019), establishment of lung compliance (Jakus et al. 2014) and growth of organ progenitor niches (Peña-Jimenez et al. 2019; Gur-Cohen et al. 2019; Liu et al. 2020; Yoon et al. 2019). Accordingly, therapeutic manipulation of lymphatics has shown efficacy in animal models of lymphedema (Szőke et al. 2021; Yoon et al. 2003), myocardial infarction (Henri et al. 2016; Klotz et al. 2015; Vieira et al. 2018), malignancy (Hu et al. 2020; Song et al. 2020), neurodegeneration (Da Mesquita et al. 2021; Da Mesquita, Louveau, et al. 2018), and cystic kidney disease (Huang et al. 2016).

Despite these advances in animal studies, our understanding of lymphatic biology in human organs, and methods to target lymphatics clinically, are limited. Given the importance of tissue fluid composition in kidney physiology and function, a greater understanding of renal lymphatic in humans is needed. The human kidney contains epithelial nephrons which, allied with specialised capillary vasculature (Dumas et al. 2021; Jourde-Chiche et al. 2019), regulate plasma ultrafiltration, bodily fluid homeostasis, acid-base balance, blood pressure and several endocrine systems. A network of lymphatics exist within the kidney (Russell et al. 2019; Donnan et al. 2021; Jafree and Long 2020), present from at least the end of the first trimester in human fetal development and residing within the organ's hilum and cortex (Jafree et al. 2019). From immunohistochemical studies, lymphangiogenesis has been recognised as a common feature of human kidney diseases (Heller et al. 2007; Sakamoto et al. 2009; Kerjaschki et al. 2004; Stuht et al. 2007; Tsuchimoto et al. 2017; Adair et al. 2007; Rodas et al. 2022). A more detailed assessment of human kidney lymphatic structure, molecular features and associations with other cell types may help to explain why, despite

the postulated role of lymphatic expansion in the resolution of inflammation, immune infiltration, fibrosis and deterioration of organ function still occur in renal pathologies.

Here, we utilised immunostaining of large tissue samples to delineate the three-dimensional (3D) architecture of lymphatics in human kidneys, marrying this with single-cell RNA sequencing (scRNA-seq) to reveal the hierarchical arrangement of human kidney lymphatics and their organ-specific transcriptional features. We then interrogate chronic alloimmune rejection, featuring interstitial fibrosis and tubular atrophy; a leading cause of late allograft failure (Hariharan et al. 2021; Clayton et al. 2019) and associated with allograft lymphatic expansion with unknown consequences (Wong 2020). The alterations to lymphatic architecture we found in chronic rejection, occurring alongside defective trafficking of and molecular crosstalk with effector T cells, together implicate lymphatic dysfunction as a hallmark of alloimmunity with potential therapeutic implications.

RESULTS AND DISCUSSION

Characterisation of lymphatic vessel architecture, spatial relationships and molecular profile in the human kidney

We first characterised kidney lymphatic architecture in humans by obtaining kidney tissue from four deceased organ donors (**Table S1A**). Tissues were immunolabelled with a D2-40 monoclonal antibody targeting the transmembrane protein, podoplanin (PDPN) (Kahn et al. 2002), before confocal or lightsheet fluorescence microscopy (LSFM); techniques used to visualise kidney lymphatics during organogenesis (Jafree et al. 2019) and in murine disease models (Liu et al. 2021). PDPN$^+$ vessel networks were discriminated in intact volumes of human kidney cortex up to 3 mm^3 (**Fig.1A**). Mapping vessel radius revealed the structural hierarchy of human kidney lymphatics, with the smallest vessels at the initiation of the lymphatic network (radius ~3.5 µm) arising in the cortex in confluence with larger vessels (radius ~50 µm) at the corticomedullary junction (**Fig.1B**). These vessels co-stained for the canonical lymphatic marker (Banerji et al. 1999; Wigle and Oliver 1999) the transcription factor prospero homeobox protein 1 (PROX1), with nuclear PROX1$^+$ localisation evident within PDPN$^+$ lymphatics (**Fig.1C**). However, expression of the transmembrane glycoprotein lymphatic vessel endothelial hyaluronan receptor 1 (LYVE1) was sparse and limited to lymphatic vessel tips (**Fig.1D**).

We then assessed the precise anatomical location of lymphatic vessels relative to differentiated renal structures in the human kidney. Counterstaining to delineate nephron tubular epithelia, segments, including *Lotus tetragonolobus* lectin (LTL), which binds proximal tubular apical membranes within the cortex, and uromodulin (UMOD), expressed by loop of Henle epithelium in the medulla, confirmed PDPN$^+$ blind-ended lymphatics in the renal cortex (**Fig.1E**) and their absence in the medulla (**Fig.1F**), consistent with previous studies (Ishikawa et al. 2006; Sakamoto et al. 2009; Kerjaschki et al. 2004; Stuht et al. 2007; Adair et al. 2007; Tsuchimoto et al. 2017). Lymphatics have been described in the sub-capsular space around the kidney (Holmes et al. 1977; Russell et al. 2019), but this was not

evident in our samples, despite the capsule being left intact (**Fig.1G**). Within the renal cortex, PDPN$^+$ lymphatics follow the course of UAE-I$^+$ arterioles *en route* to glomeruli (**Fig.1H**); the site of plasma ultrafiltration, before giving off terminal branches adjacent to major sites of reabsorption of solute, ions and drugs, including megalin (LRP2)$^+$ proximal tubules (**Fig.1I**) and calbindin 1 (CALB1)$^+$ distal tubules (**Fig.1J**). Lymphatics then continue towards the kidney hilum adjacent to medullary *Dolichos biflorus* agglutinin (DBA)$^+$ collecting ducts (**Fig.1K**). A model of these findings is presented in **Fig.1L**.

Lymphatics represent a rare cell type within the kidney. Therefore, to generate molecular profiles of human kidney lymphatics, we integrated published scRNA-seq data from 59 kidneys with additional data generated from five further samples (**Fig.2A**). This integrated kidney cell atlas contained 217,411 human kidney cells, including 151,038 'control' cells from living donor biopsies or non-tumorous regions of tumour nephrectomies and 66,373 cells from diseased samples, including chronic kidney disease (CKD) and different aetiologies of transplant rejection (**Fig.S1A**). We identified 37 transcriptionally distinct clusters (**Fig.S1B**), including a lymphatic cluster (n = 700) distinct from five other blood endothelial clusters. We first examined cells from control samples to curate a lymphatic transcriptional signature, comprising 227 differentially expressed genes (DEG), that included those found within several relevant gene ontology (GO) gene-sets, including lymphatic fate commitment (GO:0060838, fold-enrichment > 100, $p = 1.66 \times 10^{-2}$) and lymphangiogenesis (GO:0001946, fold-enrichment = 67.4, $p = 8.37 \times 10^{-3}$). Canonical lymphatic markers including *PROX1* ($\log_2$FC = 2.97), *PDPN* ($\log_2$FC = 2.65), neuropilin 2 (*NRP2,* $\log_2$FC = 2.73) and chemokine (C-C motif) ligand (*CCL*)*21* ($\log_2$FC = 7.23) were among the top 20 DEGs in the LEC cluster (**Fig.2B**). Several postulated biomarkers of kidney disease (He et al. 2019; Tanaka et al. 2018; Shi et al. 2020) not previously known to be expressed by kidney lymphatics were identified, such as fatty acid binding protein 4 *(FABP4*, $\log_2$FC = 5.69) trefoil factor 3 (*TFF3,* $\log_2$FC = 5.58) and angiopoietin 2 (*ANGPT2*, $\log_2$FC = 2.46) (**Fig. 2B**).

PROX1 and LYVE1 have been used to identify or target lymphatics in mouse studies of kidney disease (Donnan et al. 2021; Jafree and Long 2020) so we performed a detailed analysis of these markers in the human kidney. Our scRNA-seq data showed that *PROX1* expression was not limited to kidney lymphatics but was also evident in loop of Henle and distal convoluted tubule cells (**Fig.2B**). PROX1 expression was confirmed in E-cadherin $(CDH1)^+$ medullary tubules (**Fig.2C**), mirroring observations in mouse (Kim et al. 2015), but was not detected in vasa recta endothelial cells at transcript (**Fig.2B**) or protein level (**Fig.2D**), in contrast to murine studies (Kenig-Kozlovsky et al. 2018; Liu et al. 2021). LYVE1 was expressed by renal macrophages (**Fig.2E**) and blood vasculature (**Fig.2F**), as noted previously in both mouse (H.-W. Lee et al. 2011) and human kidney (Marshall et al. 2022). These findings demonstrate PROX1 and LYVE1 expression beyond lymphatics in the human kidney; relevant for experiments using these markers for imaging or therapeutic manipulation.

Lymphatics possess phenotypic heterogeneity, with distinction between blind-ended capillaries lacking mural cell coverage and valve-containing smooth muscle-lined collecting vessels. Akin to blood vessels, different organs may also contain molecularly and structurally distinct lymphatics (Petrova and Koh 2018; Wong et al. 2018). To investigate these properties, we first stained kidney lymphatics for α-smooth muscle actin, and found, akin to lung (Reed et al. 2019) but unlike dermis or mesentery (Wang et al. 2017), that these vessels lack smooth muscle coverage (**Fig.2G-H**). To further assess inter-organ heterogeneity and determine if kidney lymphatics have a distinct molecular profile, we compared the transcriptome of human kidney lymphatics to lymphatics isolated from published scRNA-seq data of human heart, lung and skin (**Fig.2I**). Two of the top markers of kidney lymphatics, relative to lymphatics in other organs, included deoxyribonuclease (*DNASE*)*1L3* ($\log_2$FC = 2.51, $p = 2.33 \times 10^{-39}$) and the chemokine *CCL14* ($\log_2$FC = 3.12, $p = 6.83 \times 10^{-92}$). Notably, expression of *LYVE1* in kidney lymphatics was significantly lower than in lymphatics of other organs ($\log_2$FC = -1.21, $p = 3.37 \times 10^{-20}$) (**Fig.2I**). *LYVE1*, was only

detectable in a quarter of kidney lymphatic cells, consistent with the spatial restriction of LYVE1 observed in 3D imaging (**Fig.1D**).

Taken together, our 3D imaging and scRNA-seq analyses support the organ-specificity of lymphatic structure and profile, extending these observations to the human kidney. We show human kidney lymphatics, which possess a capillary-like nature, initiate adjacent to specialised tubular epithelium in the cortex, and have a unique transcriptomic profile compared with other renal cells or lymphatics within other organs.

Structural phenotype and origin of kidney lymphatics in chronic transplant rejection and their putative targeting by alloantibodies

Several seminal studies have demonstrated expansion of intra-graft lymphatics during allograft rejection in rodent models (Palin et al. 2013; Vass et al. 2012; Lin et al. 2021; Motallebzadeh et al. 2012) and in humans (Adair et al. 2007; Kerjaschki et al. 2004; Stuht et al. 2007; Tsuchimoto et al. 2017), suggesting that these vessels are either insufficient to resolve allograft inflammation or themselves partake in the process of rejection (Wong 2020). To probe this further, we used 3D lymphatic imaging and scRNA-seq to study kidneys with chronic rejection, which frequently involves both T cell and antibody-mediated alloimmune responses, leading to allograft injury (Loupy et al. 2022; Callemeyn et al. 2022). In three allograft explants with chronic mixed (T cell- and antibody-mediated) rejection (**Table S1B**) and using organ donor tissues as controls, we found disorganisation of the lymphatic network, with loss of structural hierarchy (**Fig.3A**), a seven-fold increase in lymphatic density (95.12 ± 49.21 *vs.* 690.3 ± 121.6 vessels / mm^3, $p = 0.0014$) and infiltration of lymphatics into the kidney medulla (**Fig.3A-C**), which is normally devoid of these vessels (Donnan et al. 2021; Jafree and Long 2020; Russell et al. 2019). Additional abnormalities observed in rejection included a reduction in the mean vessel radius (10.84 ± 6.76 *vs.* 6.27 ± 3.95 µm, $p < 0.0001$) and branching angle (112.3 ± 28.87 *vs.* 101.4 ± 36.70°, $p < 0.0001$) compared to control kidneys.

This distortion of lymphatic architecture is reminiscent of the blood endothelial disruption observed in chronic rejection (Adair et al. 2007), where donor-derived endothelial cells expressing MHC Class II molecules human leukocyte antigen (HLA)-DR, HLA-DQ and HLA-DP (Kosmoliaptsis et al. 2014; Daniëls et al. 2020) are targeted by alloantibodies (Loupy and Lefaucheur 2018). To examine whether lymphatics might also be subject to alloantibody-mediated damage, we assessed the donor or recipient status of lymphatics derived from allografts with chronic rejection and compared this to healthy allografts and other non-rejection pathologies of the allograft including pyelonephritis and focal segmental glomerulosclerosis. Within our dataset, the majority of transplant lymphatic cells were donor-derived (n = 244/247, 98.8%), with a small contribution from recipient cells to lymphatics (n = 3/247, 1.2%), in line with a previous study of sex-mismatched renal allografts (Kerjaschki et al. 2006). To assess whether lymphatics might also be subject to alloantibody-mediated damage, we assessed lymphatic MHC Class II expression in the dataset. Kidney lymphatics expressed *HLA-DP* and *HLA-DR* transcripts, with little *HLA-DQ* detectable (**Fig.3F**), and *HLA-DRB5* expression was greater in kidneys with rejection than those with CKD ($\log_2$FC = 2.05, p = 1.92 x 10^{-7}). As well as being evident in $CD31^+$ blood endothelial cells (**Fig.3G**) and $CD68^+$ macrophages (**Fig.3H**), the latter previously reported (Muczynski et al. 2003; Muczynski et al. 2001), HLA-DR protein expression was confirmed on $PDPN^+$ lymphatics (**Fig.3I**). Consistent with alloantibody-mediated complement activation, we found C4d deposition on $PDPN^+$ lymphatic vessels in the cortex of transplant rejection tissues (**Fig.3J**). Overall, our data suggest that allograft lymphatics may be directly targeted by donor-specific HLA antibodies leading to complement activation, in an analogous mechanism to that described for blood vascular endothelium, potentially leading to the distorted lymphatic architecture observed in rejecting allografts.

Spatial and molecular analysis of lymphocyte trafficking by kidney lymphatics in chronically rejecting transplants

In homeostasis and inflammation, lymphatics secrete chemokines such as CCL21, generating gradients that promote leukocyte chemotaxis, entry into lymphatics and tissue efflux (Luther et al. 2002). Egress of leukocytes reduces local inflammation whilst simultaneously delivering these cells to draining lymph nodes, the sites where adaptive immune responses are generated (Johnson 2021; Steele and Lund 2021). Given the potential for lymphatics to influence alloreactive lymphocyte trafficking in chronic rejection, we investigated the localisation of PDPN$^+$ lymphatics relative to CD20$^+$ B cells and CD4$^+$ T cells, central to the adaptive alloimmune response through recognition of differences between donor and recipient histocompatibility antigens by recipient T cells and production of antibodies by the B cell lineage (Duneton et al. 2022). We built on the findings of previous immunohistochemical studies describing the presence of lymphocytes within and around rejecting allograft lymphatics (Tsuchimoto et al. 2017; Kerjaschki et al. 2004) by quantifying intraluminal and extra-lymphatic tissue lymphocytes using 3D image analysis (**Fig.4A-B**). Luminal CD20$^+$ B cell density was halved in rejecting allografts compared with controls (p = 0.0042) (**Fig.4C**), although the absolute number of B cells did not significantly differ (p = 0.977), suggesting a change in lymphatic volume rather than B cell abundance. Conversely, the total number of intra-luminal CD4$^+$ T cells increased in chronic rejection (p = 0.0032), with the mean CD4$^+$ T cell density increasing threefold (**Fig.4D**, $p < 0.0001$), higher than that of the surrounding allograft parenchyma (**Fig.4D**, mean $p < 0.0001$). To further examine the spatial interactions between lymphocyte subsets and lymphatics in transplant rejection, we assessed the normalised distance (Davis et al. 2017) of each lymphocyte to its nearest lymphatic vessel (**Fig.4E-F**). No significant spatial association was observed between CD20$^+$ B cells and lymphatics in either control kidneys (n = 703 cells; p = 0.631) or rejecting allografts (n = 2,963 cells; p = 0.326) (**Fig.4G**). In contrast, CD4$^+$ T cells (n = 2,149 cells across two controls) had a peak frequency within 0-100 μm from the nearest lymphatic vessel and showed greater spatial proximity to these vessels than would be expected if

randomly distributed (p = 0.029). This spatial proximity of CD4$^+$ T cells to lymphatics was lost in chronic transplant rejection (n = 4,382 cells , p = 0.699) (**Fig.4H**), suggesting dysregulated CD4$^+$ T cell trafficking via lymphatics.

To investigate molecular signals underpinning lymphocyte chemotaxis by lymphatics, we analysed the single-cell transcriptomes of kidney lymphatics and immune cells in isolation, including B cells and effector CD4$^+$ T cells, interrogating ligand-receptor interactions using CellPhoneDB (Efremova et al. 2020) (**Fig.S2A**). We detected ten predicted chemokine interactions between lymphatics and lymphocytes (**Fig.4I**), with the known lymphatic-leukocyte chemotactic cue mediated *via CCL21* signalling to its receptor CC receptor (*CCR)7* (Johnson 2021; Kerjaschki et al. 2004) evident across all groups. Lymphatics also expressed the atypical chemokine receptor 2 (*ACKR2*) that acts to sequester chemokines such as CCL2, CCL3, CCL4 and CCL5 and generate chemotactic gradients (Bonavita et al. 2016). These chemokines and their complementary receptors were varyingly expressed by macrophages and natural killer (NK), NKT, CD8$^+$ T, CD4$^+$ T and B cells in our scRNAseq data (**Fig.4J-K**). In rejection, there was a significant increase in the predicted interaction mediated by *ACKR2* on lymphatics and B cell-derived *CCL4* (**Fig.4I**). In contrast, a number of *ACKR2*-mediated interactions between lymphatics and effector CD4$^+$ T cells were lost in rejection compared to control tissues and CKD, particularly *ACKR2-CCL2, -CCL14* and -*CCL28* (**Fig.4I**). These molecular analyses suggest a broad role for lymphatics in regulating kidney leukocyte dynamics. Attenuation of atypical chemokine interactions may underpin the disrupted localisation of CD4$^+$ T cells observed in our 3D imaging of rejecting kidneys, analogous to the aberrant accumulation of immune cells within lymphatics present in ACKR2-deficient mice (K. M. Lee et al. 2011).

Putative immunomodulation of *in situ* adaptive immune responses by lymphatics in alloimmunity

Whether lymphatics propagate or inhibit alloimmunity in transplantation is controversial (Wong 2020; Vass et al. 2009). On one hand, expansion of lymphatics and their proximity to immune cell aggregates has been associated with improved graft survival, potentially due to increased leukocyte clearance from the kidney (Tsuchimoto et al. 2017; Stuht et al. 2007; Pedersen et al. 2020), whereas other studies found increased lymphatics in kidneys with greater fibrosis and immune activation (Palin et al. 2013; Vass et al. 2012; Talsma et al. 2017; Lin et al. 2021; Thaunat et al. 2006). To investigate how adaptive immune responses within human kidney allografts might be modulated by lymphatics, we profiled tertiary lymphoid structures (TLS); aggregates of lymphocytes capable of *in situ* activation of antigen-specific T cells (Lee et al. 2022; Dorraji et al. 2020; Sato et al. 2020; Ichii et al. 2022; Meylan et al. 2022; Schröder et al. 1996; Lee et al. 2006) and observed in proximity to lymphatics in immunohistochemical studies of rejecting and non-rejecting allografts (Stuht et al. 2007; Kerjaschki et al. 2004; Tsuchimoto et al. 2017). In addition to observing PDPN$^+$ lymphatics in close proximity to T and B cell-containing aggregates within the cortex of rejecting allografts (**Fig.5A**), we dissected the spatiotemporal relationship between TLS and lymphatics using CD21, a follicular dendritic cell marker, to identify TLS, and peripheral lymph node addressin (PNAd), to delineate high endothelial venules (HEV); only present in late-stage TLS (Ruddle 2016; Robson and Kitching 2020; Sato et al. 2021; Drayton et al. 2006; Alsughayyir et al. 2017; Motallebzadeh et al. 2012) (**Fig.5B**). We found PDPN$^+$ lymphatics in TLS of all stages (n = 9/9, 100%), whereas HEVs were only present in half of TLS (n = 5/9, 55.6% p = 0.023). In these late-stage TLS, PDPN$^+$ lymphatic vessel tips were localised more closely than HEVs to the CD21$^+$ TLS core (**Fig.5C,** mean distance = 49.53 ± 23.83 μm *vs.* 109.6 ± 25.13 μm, 95% CI = 24.33-95.76, p = 0.0047). Furthermore, an interconnected network of PDPN$^+$ lymphatics joined adjacent TLS, whereas PNAd$^+$ HEVs were limited to the vicinity of TLS (**Fig.5D**). Lymphatics and HEV cells were also transcriptionally distinct (**Fig.5E**); lymphatics expressed a number of anti-inflammatory, pro-

reparative transcripts (Paulsen et al. 2008; Belle et al. 2019; Liu et al. 2020), including *TFF3* and reelin (*RELN*). Conversely, HEV cells expressed molecules involved in leukocyte recruitment and activation such as *CXCL16* (Di Pilato et al. 2021), fractalkine (*CX3CL1*) (Garcia et al. 2013), CD40 (Elgueta et al. 2009) and interleukin 32 *(IL32*) (de Albuquerque et al. 2020) (**Fig.5F**). To further explore potential anti-inflammatory roles of lymphatics, we assessed immune stimulatory or inhibitory interactions between lymphatics and $CD4^+$ T cell subsets, including effector, naïve and regulatory T cells. Co-inhibitory molecular interactions that dampen effector T cell responses (Anderson et al. 2016), including the ligands poliovirus receptor (*PVR*) and galectin 9 (*LGALS9*), dominated between lymphatics and $CD4^+$ T cell subsets (**Fig. 5G**) or $CD8^+$ T cells (**Fig.S2B**). The predicted immune-inhibitory interactions mediated by *PVR* and *LGALS9* were also present in CKD and non-rejecting transplant kidneys (**Fig.S2C-D**), but to a lesser extent than in chronic rejection (**Fig.5H**). We confirmed PVR expression by $PDPN^+$ lymphatics in transplants with chronic rejection and found $CD4^+$ T cells directly contacting PVR^+ regions of lymphatic vessels (**Fig.5I**).

Collectively, 3D imaging and scRNA-seq analyses implicate lymphatics as an early and ubiquitous feature of lymphoid aggregates in kidneys with chronic rejection, forming an interconnecting vascular network between TLS. Lymphatics display a distinct molecular profile from their blood vascular counterparts in chronic rejection, expressing immune inhibitory molecules with the potential to regulate local alloreactive $CD4^+$ T cells. These findings, akin to those recently delineated for mouse tumour (Gkountidi et al. 2021; Steele et al. 2022), central nervous system (Hsu et al. 2022) and dermal lymphatics (Churchill et al. 2022), suggest lymphatics modulate adaptive immune responses within the tissue microenvironment, beyond their roles in leukocyte egress; implicating these vessels as an emerging therapeutic target in chronic transplant rejection (Gupta et al. 2012; Sun et al. 2021).

CONCLUSION

Overall, we have used 3D imaging and scRNA-seq to comprehensively characterise the human kidney lymphatic vasculature, providing spatial and molecular references for studies of kidney physiology and disease. We also provide new insights into the potential roles of lymphatics in transplant biology and immunity, pointing towards putative alloantibody targeting of lymphatics, accompanied by loss of lymphatic hierarchy and impairment of $CD4^+$ T cell lymphatic trafficking as cellular hallmarks of chronic transplant rejection. These findings potentially explain why loss of graft function occurs despite lymphangiogenesis. Finally, we decipher relationships between kidney lymphatics and alloimmune responses, identifying that these vessels colonise and interconnect tertiary lymphoid niches and may partake in immunoregulatory crosstalk involving co-inhibitory checkpoint molecules. Such findings provide impetus to consider lymphatics as a key player in alloimmunity with therapies modulating lymphatics having potential to promote transplant longevity.

ACKNOWLEDGEMENTS

The authors would like to acknowledge Professors Lucy Walker, Mark Lythgoe, Alan Salama (UCL) and Dr René Hägerling (Charité Universitätsmedizin Berlin) for their ongoing support and valuable discussions about the work, and Dr Kelvin Tuong (University of Cambridge) for producing scripts for visualisation and analysis of ligand-receptor pair analysis of scRNA-seq data (https://github.com/zktuong/ktplots). Surgical explantation was performed by the Renal Transplant surgical team at Royal Free Hospital, London, UK. Confocal microscopy was performed at the Light Microscopy Core Facility at UCL GOSICH and LSFM was performed at the UKRI Dementia Research Institute. All work was performed with the support of a grant from Kidney Research UK (IN_012_20190306), a Rosetrees Trust PhD Plus Award (PhD2020\100012) and Foulkes Foundation Fellowship to Dr Daniyal Jafree, a Wellcome Trust Investigator Award (220895/Z/20/Z) to Professor David Long, the National Institute for Health Research (NIHR) Biomedical Research Centre at Great Ormond Street Hospital for Children NHS Foundation Trust and University College London. All authors declare no conflicts of interest.

AUTHOR CONTRIBUTIONS

DJJ, MRC, RM and DAL were involved in the conception of the study. Acquisition of material and laboratory experiments were performed by DJJ, MKJ, LGR, LMR, WJM, BIL, LW, TA, SM, JC, KC and KP. Analysis of 3D images or scRNA-seq data was performed by DJJ, BS, BD, HM, DM, NH, CW and SWS. Histopathological analysis and acquisition of clinical data was performed by LH and RM. Project oversight and supervision was provided by PJDW, MAB, PJS, MRC, RM, ASW and DAL. DJJ wrote the first draft of the paper, refined by DAL and MRC, and subsequently all authors were involved in revision and preparation of the final manuscript for submission.

FIGURES AND FIGURE LEGENDS

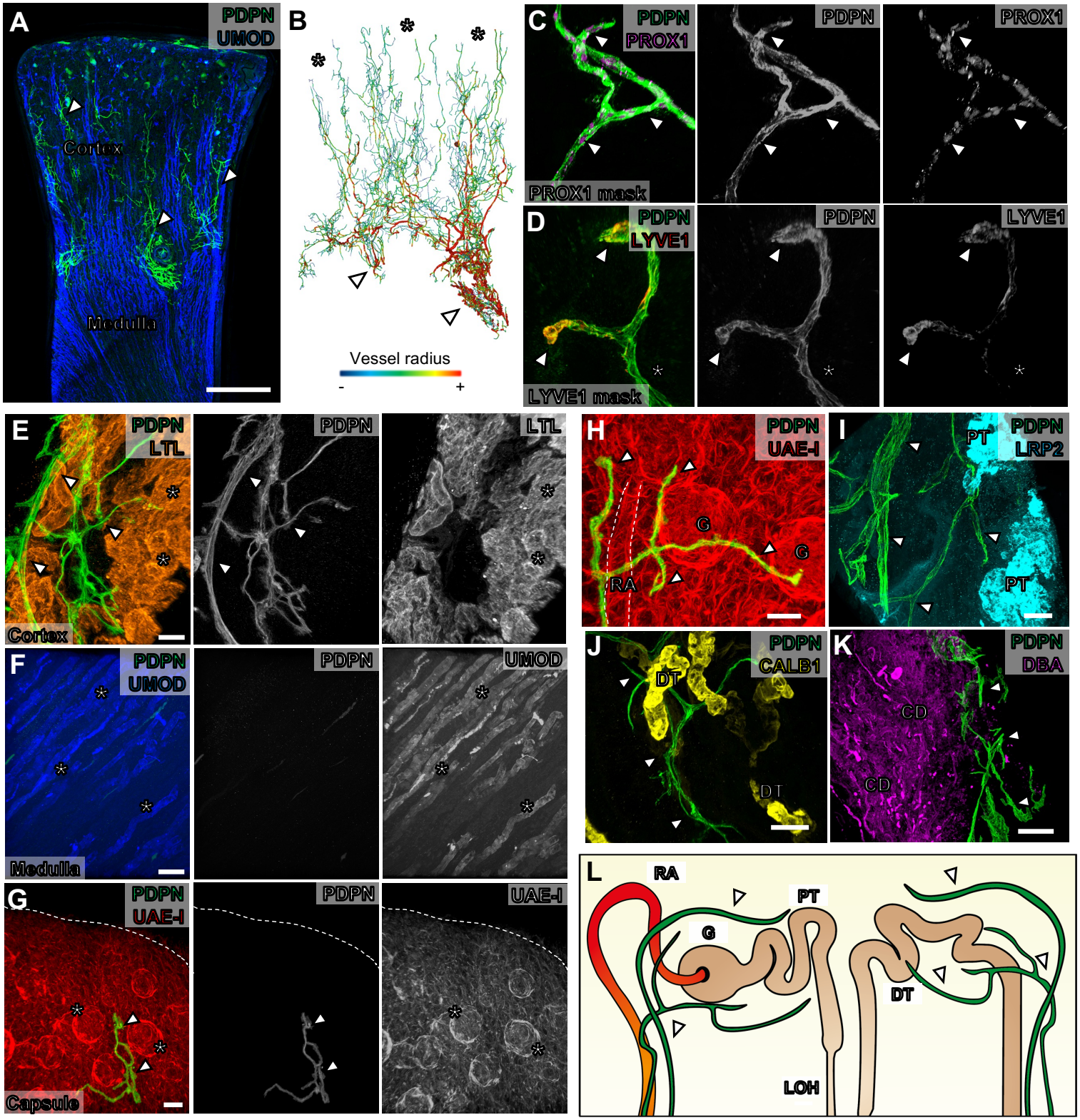

Figure 1. Three-dimensional imaging of lymphatics and their spatial relationships in the human kidney

(A) Representative maximum intensity *z*-projection, from low-resolution confocal tile scans, of *n* = 3 human kidney tissues labelled for podoplanin (PDPN) and uromodulin (UMOD), demonstrating PDPN$^+$ lymphatics (arrowheads). Scale bar = 2000 µm. **(B)** Segmented and rendered LSFM imaging of lymphatics from the same kidney tissue in **A**, representative of *n* = 3 images. 3D colour renderings represent vessel branch radii, with blue representing the smallest radius (< 3.5 µm, asterisks) and red representing the largest radii (> 18 µm, arrowheads). **(C-D)** Representative 3D reconstruction of cortical regions from *n* = 2 human kidney tissues labeled for PDPN and either prospero homeobox protein 1 (PROX1) or lymphatic vessel endothelial hyaluronan receptor 1 (LYVE1). The PROX1 and LYVE1 signals are masked to only include expression from within the vessel, demonstrating expression of PDPN$^+$ cells. Sparse membrane localization of LYVE1 is demonstrated (arrowheads). Representative of five regions of interest imaged. Scale bars = 30 µm. **(E-G)** Regional localization of lymphatics (arrowheads) in the human kidney using *Lotus tetragonolobus* lectin (LTL, cortex), UMOD (medulla) and *Ulex europaeus* agglutinin I (UEA-I, dotted lined delineating the capsule). Regional structures are indicated with asterisks, including proximal tubules in **E**, loops of Henle in **F** and glomeruli in **G**. Scale bars = 70 µm **(E)**, 150 µm **(F)**, 100 µm **(G)**. **(H-K)** Spatial relationships of lymphatics (arrowheads) relative to UAE-I$^+$ renal arterioles (RA) and glomeruli (G) in **H**, megalin (LRP2)$^+$ proximal tubules (PT) in **I**, calbindin (CALB1)$^+$ distal tubules (DT) in **J** and *Dolichos biflorus* agglutinin (DBA)$^+$ collecting ducts (CD) in **K**. Scale bars = 50 µm **(H)**, 80 µm **(I** and **J)**, 300 µm **(K)**. **(L)** Schematic depicting the spatial relationships of lymphatics (arrowheads) to nephron segments. All imaging from **E-K** representative of five regions of interest imaged across *n* = 2 kidneys.

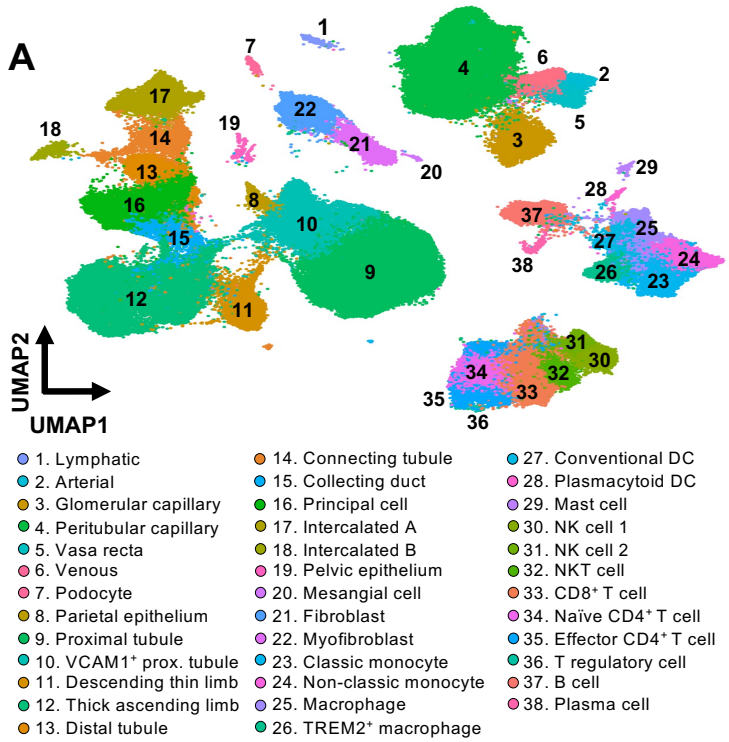
A
UMAP2
UMAP1
1. Lymphatic
2. Arterial
3. Glomerular capillary
4. Peritubular capillary
5. Vasa recta
6. Venous
7. Podocyte
8. Parietal epithelium
9. Proximal tubule
10. VCAM1+ prox. tubule
11. Descending thin limb
12. Thick ascending limb
13. Distal tubule
14. Connecting tubule
15. Collecting duct
16. Principal cell
17. Intercalated A
18. Intercalated B
19. Pelvic epithelium
20. Mesangial cell
21. Fibroblast
22. Myofibroblast
23. Classic monocyte
24. Non-classic monocyte
25. Macrophage
26. TREM2+ macrophage
27. Conventional DC
28. Plasmacytoid DC
29. Mast cell
30. NK cell 1
31. NK cell 2
32. NKT cell
33. CD8+ T cell
34. Naïve CD4+ T cell
35. Effector CD4+ T cell
36. T regulatory cell
37. B cell
38. Plasma cell

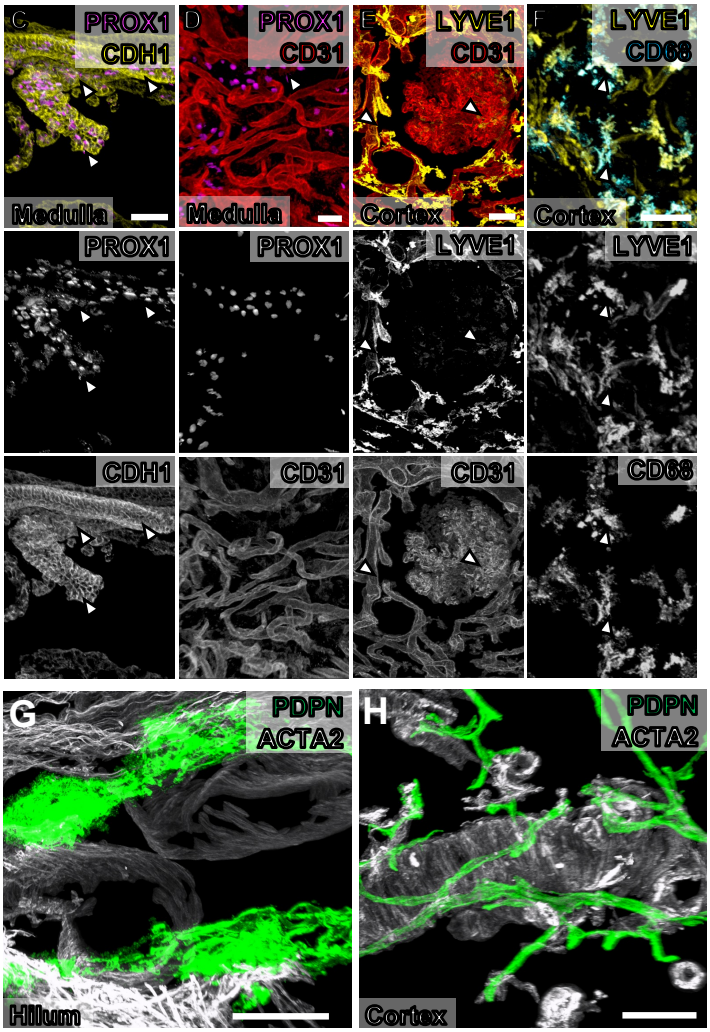
C PROX1 CDH1 Medulla
D PROX1 CD31 Medulla
E LYVE1 CD31 Cortex
F LYVE1 CD68 Cortex
PROX1
PROX1
LYVE1
LYVE1
CDH1
CD31
CD31
CD68
G PDPN ACTA2 Hilum
H PDPN ACTA2 Cortex

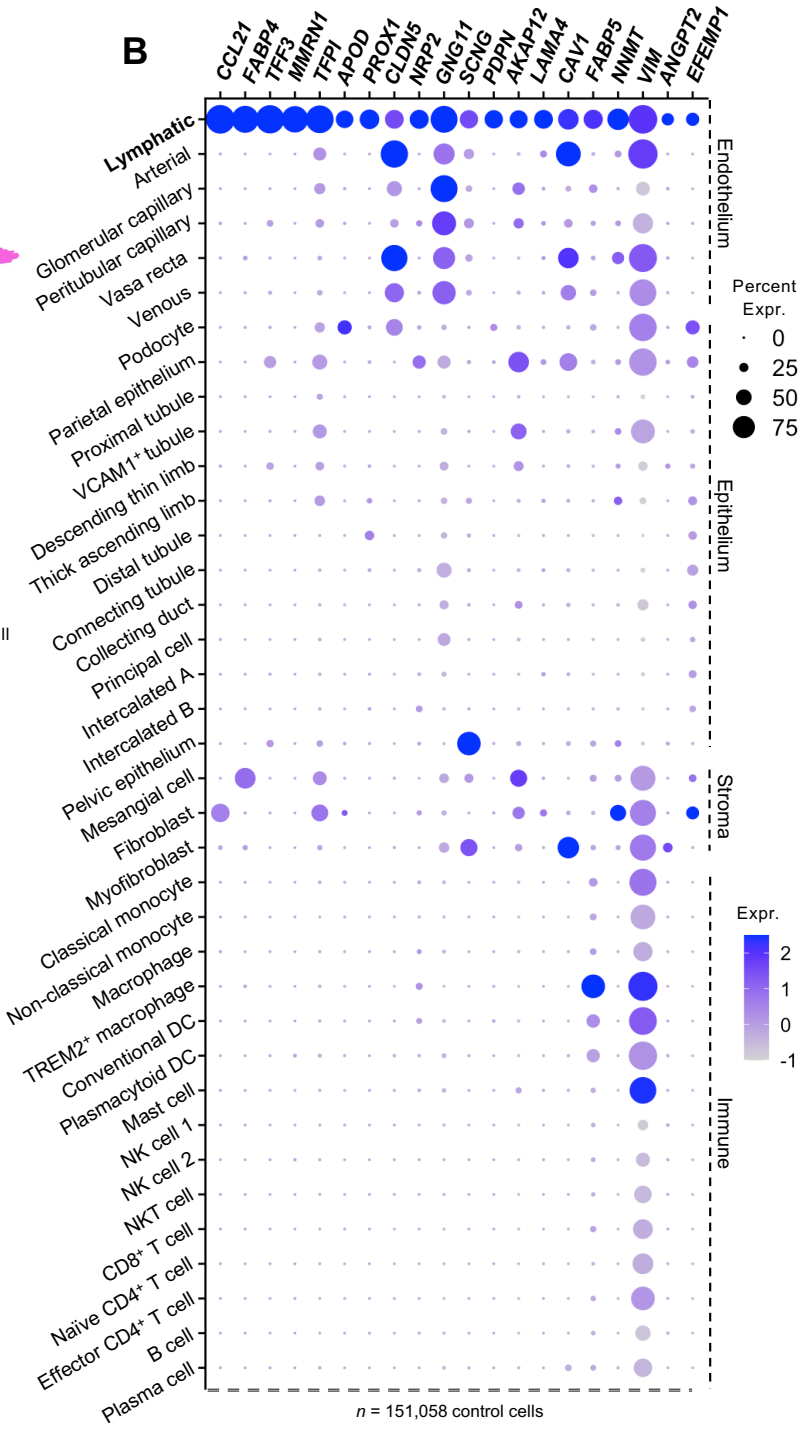
B
CCL21
FABP4
TFF3
MMRN1
TFPI
APOD
PROX1
CLDN5
NRP2
GNG11
SCNG
PDPN
AKAP12
LAMA4
CAV1
FABP5
NNMT
VIM
ANGPT2
EFEMP1
Lymphatic
Arterial
Glomerular capillary
Peritubular capillary
Vasa recta
Venous
Podocyte
Parietal epithelium
Proximal tubule
VCAM1+ tubule
Descending thin limb
Thick ascending limb
Distal tubule
Connecting tubule
Collecting duct
Principal cell
Intercalated A
Intercalated B
Pelvic epithelium
Mesangial cell
Fibroblast
Myofibroblast
Classical monocyte
Non-classical monocyte
Macrophage
TREM2+ macrophage
Conventional DC
Plasmacytoid DC
Mast cell
NK cell 1
NK cell 2
NKT cell
CD8+ T cell
Naïve CD4+ T cell
Effector CD4+ T cell
B cell
Plasma cell
Endothelium
Epithelium
Stroma
Immune
Percent Expr.
0
25
50
75
Expr.
2
1
0
-1
n = 151,058 control cells

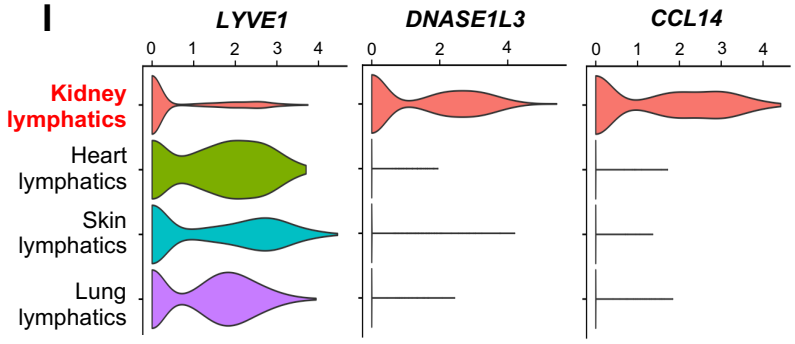
I
LYVE1
DNASE1L3
CCL14
Kidney lymphatics
Heart lymphatics
Skin lymphatics
Lung lymphatics

Figure 2. Profiling lymphatics and their molecular markers through single-cell RNA-sequencing of the human kidney

(A) Uniform manifold approximation and projection (UMAP) of an integrated atlas of 217,411 cells, including 151,058 'control' cells from live biopsies or nephrectomies, 46,540 cells from different aetiologies of transplant rejection and 19,813 chronic kidney disease. DC, dendritic cell; NK, natural killer; TREM, triggering receptor expressed on myeloid cells 2; VCAM1, vascular cell adhesion protein 1. **(B)** Dot plot of top 20 markers of lymphatics profiled across all 'control' cell types in the atlas. Categorisation for each cell type is shown on the right. **(C-F)** Analysis of non-lymphatic expression of PROX1 and LYVE1 using 3D imaging. Arrowheads the show the expression of each marker relative to cadherin 1 (CDH1)$^{+}$ medullary tubules **(C)**, CD31^{+} vasa recta **(D)** or peritubular capillaries **(E)** and CD68^{+} macrophages **(F)**. Scale bars = 50 µm (**C, E, F**), 30 µm (**D**). **(G-H)** Examination of α-smooth muscle actin (ACTA2) expression relative to PDPN^{+} lymphatics (arrowheads) in the renal hilum (**G**) and cortex (**H**). Scale bars = 50 µm (**G**), 100 µm (**H**). (**I**) Cross-organ comparison of lymphatics in the kidney, heart, skin and lung, represented by violin plots. Compared to other organs, kidney lymphatics express significantly lower *LYVE1* ($\log_2$FC = -1.21, p = 3.37 x 10^{-20}) and higher deoxyribonuclease 1L3 (*DNASE1L3;* $\log_2$FC = 2.51, p = 2.33 x 10^{-39}) and chemokine (C-C motif) ligand 14 (*CCL14;* $\log_2$FC = 3.12, p = 6.83 x 10^{-92}) expression.

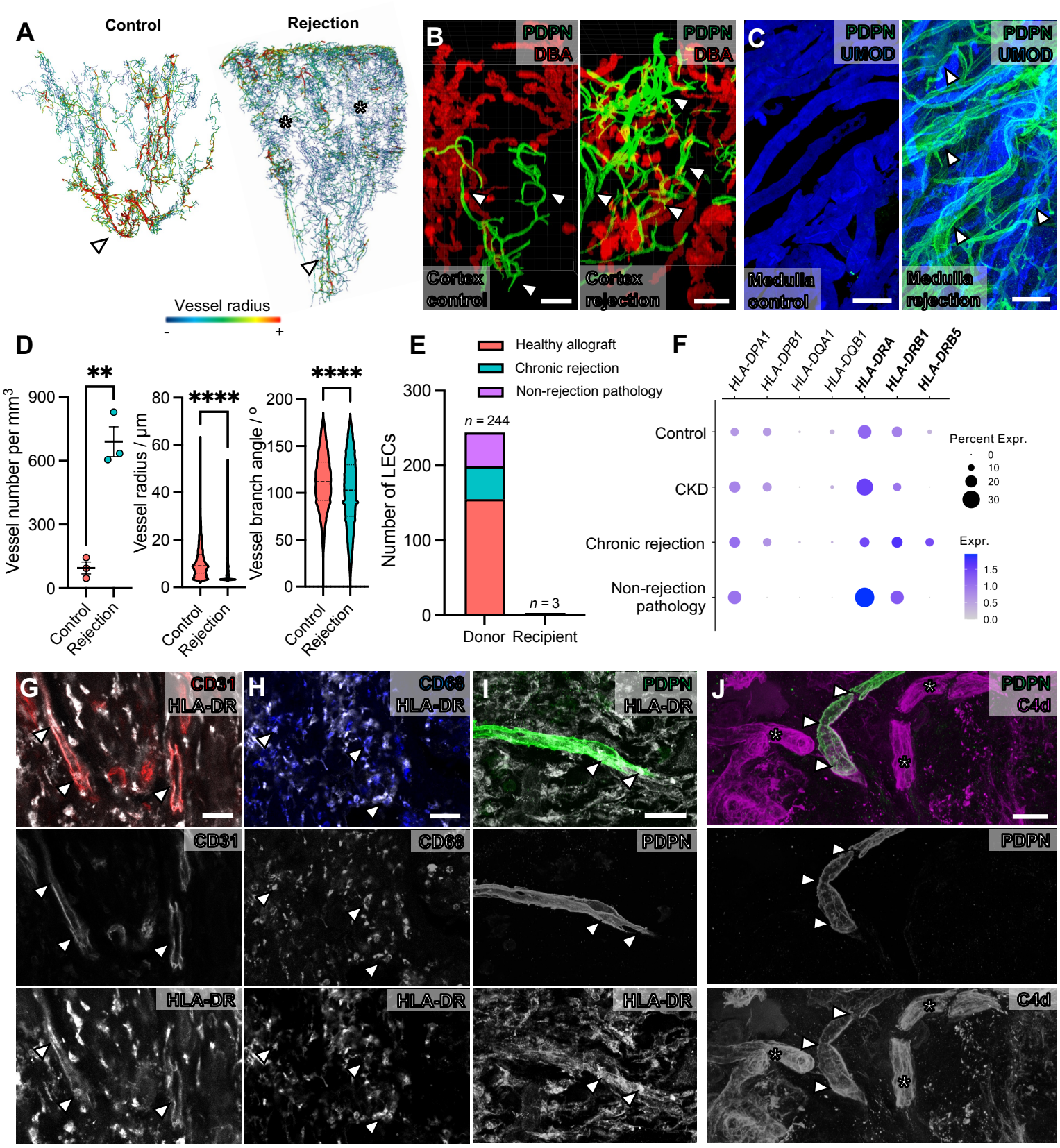
A
Control
Rejection
Vessel radius
-
+
B
PDPN
DBA
Cortex control
Cortex rejection
C
PDPN
UMOD
Medulla control
Medulla rejection
D
Vessel number per mm3
Vessel radius / µm
Vessel branch angle / °
**
****
Control
Rejection
E
Healthy allograft
Chronic rejection
Non-rejection pathology
Number of LECs
n = 244
n = 3
Donor
Recipient
F
HLA-DPA1
HLA-DPB1
HLA-DQA1
HLA-DQB1
HLA-DRA
HLA-DRB1
HLA-DRB5
Control
CKD
Chronic rejection
Non-rejection pathology
Percent Expr.
Expr.
G
CD31
HLA-DR
H
CD68
I
PDPN
J
C4d

Figure 3. Mapping structure of lymphatics in chronic kidney transplant rejection and evidence for their targeting by alloantibodies

(A) 3D renderings LSFM imaging of kidney lymphatics in control (organ donor) and chronic transplant rejection tissues, representative of *n* = 3 images per group, where colour represents vessel branch radii, with blue representing the smallest radius (smallest radius in blue < 3.5 µm; asterisks, largest radius in red, > (>18 µm, arrowheads). **(B-C)** Confocal imaging of lymphatics (arrowheads) in the renal cortex, adjacent to DBA$^+$ tubules (**B**) and medulla, adjacent to UMOD$^+$ tubules (**C**), demonstrating the expansion of lymphatics in the cortex and their infiltration into the medulla. Images are representative of six regions of interest samples across *n* = 3 kidneys per condition. Scale bars = 200 µm (**B**), 100 µm (**C**). (**D**) Quantitative analysis of lymphatic vessel branch metrics in control and rejected kidneys. Data are presented either on the level of each kidney (scatterplot, *n* = 3 per group) or with all vessels from all kidneys pooled (violin plots, *n* = 75,036 vessel branches from donor *vs.* n = 1,048,576 vessel branches in rejection). Unpaired *t*-test revealed a significant increase in the number of vessels per unit volume in rejection, (95.12 ± 49.21 *vs*. 690.3 ± 121.6 vessels / mm^3, $p = 0.0014$) whereas Mann-Whitney U tests revealed shifts in the distribution of vessel branch radius ($p < 0.0001$) and angle ($p < 0.0001$). (**E**) Donor or recipient status of the lymphatics in allograft tissues from the scRNA-seq atlas. Cells are grouped by healthy allograft, chronic rejection or non-rejection pathology of allografts (pyelonephritis, focal segmental glomerulosclerosis). (**F**) Dot plot of the expression of transcripts encoding MHC class II molecules within lymphatics, with enrichment of human leukocyte antigen (*HLA*)-*DRB5* expression in alloimmune rejection ($\log_2$FC = 2.05, $p = 1.92 \times 10^{-7}$). (**H-I**) 3D confocal images of HLA-DR expression (arrowheads) in PECAM1$^+$ endothelia (**G**), CD68$^+$ macrophages (**H**) and PDPN$^+$ lymphatics (**I**). Images are representative of five regions imaged across *n* = 2 kidneys with chronic transplant rejection. (**J**) 3D Confocal images showing deposition of complement component C4d, representative of five regions imaged across *n* = 2 kidneys with chronic transplant rejection. C4d deposition is observed in PDPN$^+$ lymphatics (arrowheads) and presumptive blood capillaries (asterisks). All scale bars = 30 µm.

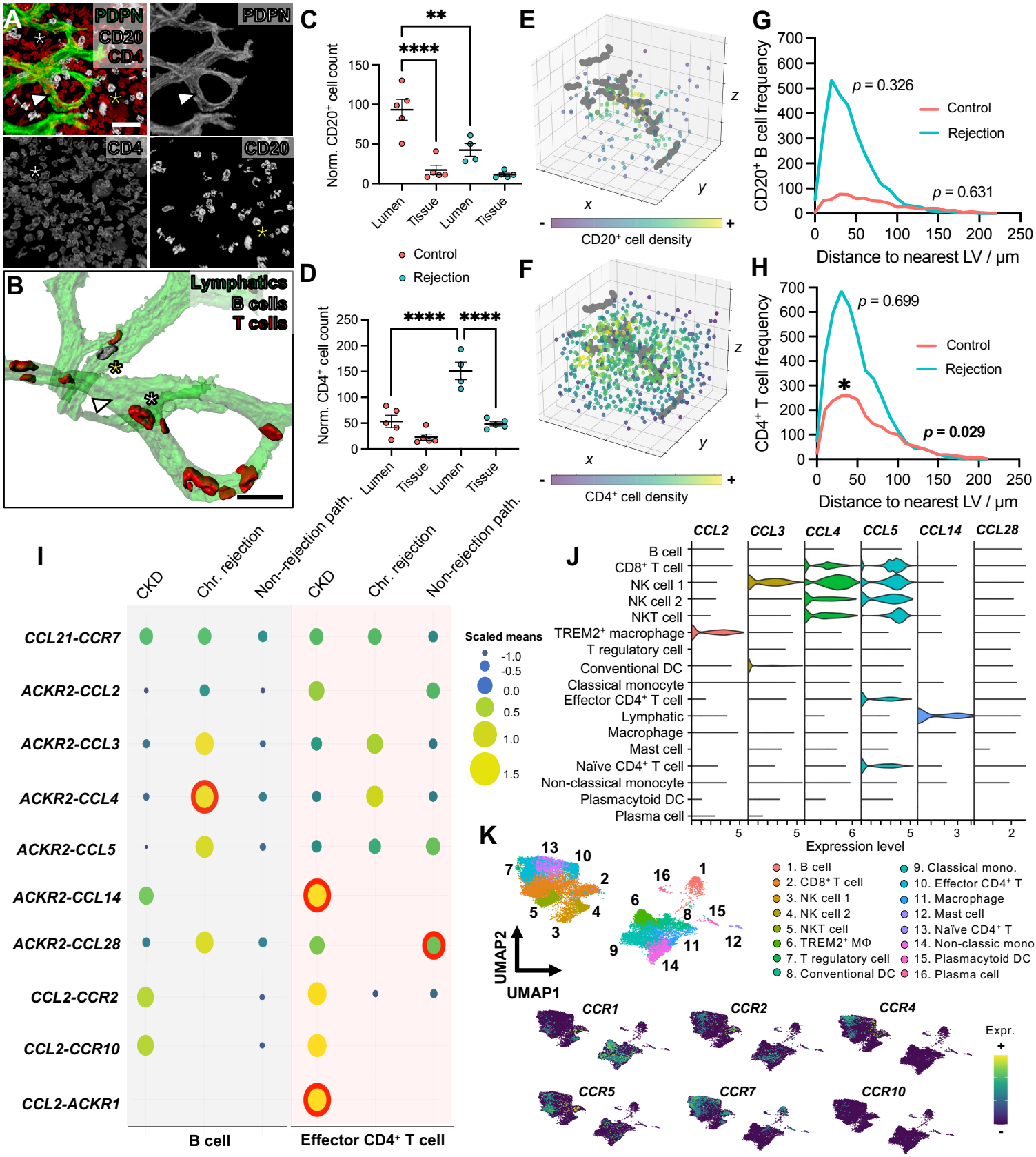
A
PDPN
CD20
CD4
B
Lymphatics
B cells
T cells
C
Norm. CD20⁺ cell count
Lumen
Tissue
Control
Rejection
D
Norm. CD4⁺ cell count
Non-rejection path.
E
CD20⁺ cell density
F
CD4⁺ cell density
G
CD20⁺ B cell frequency
p = 0.326
p = 0.631
Distance to nearest LV / µm
H
CD4⁺ T cell frequency
p = 0.699
p = 0.029
I
CKD
Chr. rejection
Non-rejection path.
CCL21-CCR7
ACKR2-CCL2
ACKR2-CCL3
ACKR2-CCL4
ACKR2-CCL5
ACKR2-CCL14
ACKR2-CCL28
CCL2-CCR2
CCL2-CCR10
CCL2-ACKR1
Scaled means
B cell
Effector CD4⁺ T cell
J
CCL2
CCL3
CCL4
CCL5
CCL14
CCL28
B cell
CD8⁺ T cell
NK cell 1
NK cell 2
NKT cell
TREM2⁺ macrophage
T regulatory cell
Conventional DC
Classical monocyte
Effector CD4⁺ T cell
Lymphatic
Macrophage
Mast cell
Naïve CD4⁺ T cell
Non-classical monocyte
Plasmacytoid DC
Plasma cell
Expression level
K
UMAP1
UMAP2
1. B cell
2. CD8⁺ T cell
3. NK cell 1
4. NK cell 2
5. NKT cell
6. TREM2⁺ MΦ
7. T regulatory cell
8. Conventional DC
9. Classical mono.
10. Effector CD4⁺ T
11. Macrophage
12. Mast cell
13. Naïve CD4⁺ T
14. Non-classic mono.
15. Plasmacytoid DC
16. Plasma cell
CCR1
CCR2
CCR4
CCR5
CCR7
CCR10
Expr.

Figure 4. Inferring the spatial and molecular basis of lymphocyte trafficking by kidney lymphatics in alloimmunity

(**A & B**) Segmented (**A**) and rendered (**B**) confocal images of PDPN$^+$ lymphatics (white arrow), CD20$^+$ B cells (yellow asterisk) and CD4$^+$ T cells (white asterisk). In **B**, the transparency of rendered lymphatics is increased to visualize intra-luminal B cells and T cells. Scale bars = 30 µm. (**C & D**) Number of intra-luminal CD20$^+$ B cells (**C**) or CD4$^+$ T cells (**D**), normalised by volume, was quantified and compared to that of the tissue parenchyma. Each point represents one volume of interest imaged. Luminal CD20$^+$ B cell density in controls (organ donor) was significantly higher than that of the tissue parenchyma (mean difference = 76.2, 95% CI = 42.9-109.4, $p < 0.0001$), and approximately halved in rejecting allografts (mean difference = 50.8, 95% CI = 15.6-86.1, $p = 0.0042$). Intraluminal CD4$^+$ T cell count was significantly higher in rejection (mean difference = 97.7, 95% CI = 52.8-142.7, $p < 0.0001$) and, within rejection, was higher than that of the surrounding parenchyma (mean difference = 102.7, 95% CI = 57.6-147.6, $p < 0.0001$). (**E & F**) Spatial point-patterns of peri-lymphatic CD20$^+$ cell (**E**) or CD4$^+$ cell (**F**) density, where lymphatic branch points represent grey dots and CD20$^+$ cells are colour-coded according to their density around the lymphatic network. **(G & H)** Histograms of CD20$^+$ cell (**G**) or CD4$^+$ T cell (**H**) frequency as a function of distance from the nearest lymphatic vessel. *p* values demonstrate whether lymphocytes are clustered around lymphatics greater than would be expected under complete spatial randomness. The only significant association observed was between CD4$^+$ T cells and lymphatics in control kidneys ($p = 0.029$). (**I**) CellPhoneDB dot plot of scRNA-seq data demonstrating top 10 chemokine interactions between lymphatics and B cells or effector CD4$^+$ T cells, partitioned by disease aetiology. Dot size represents the scaled mean expression of the interaction, and those encircled with a red ring are deemed statistically significant by CellPhoneDB. **(J)** Violin plots of transcripts encoding atypical chemokine receptor 2 (ACKR2) ligands across all immune cell types within the chronic transplant rejection scRNA-seq dataset. **(K)** UMAP of all immune cell subsets with feature plots showing expression of receptors for ACKR2 ligands across these cell types. All imaging data is representative of $n = 5$ imaging volumes each acquired from $n = 2$ allografts with chronic rejection and $n = 2$ controls.

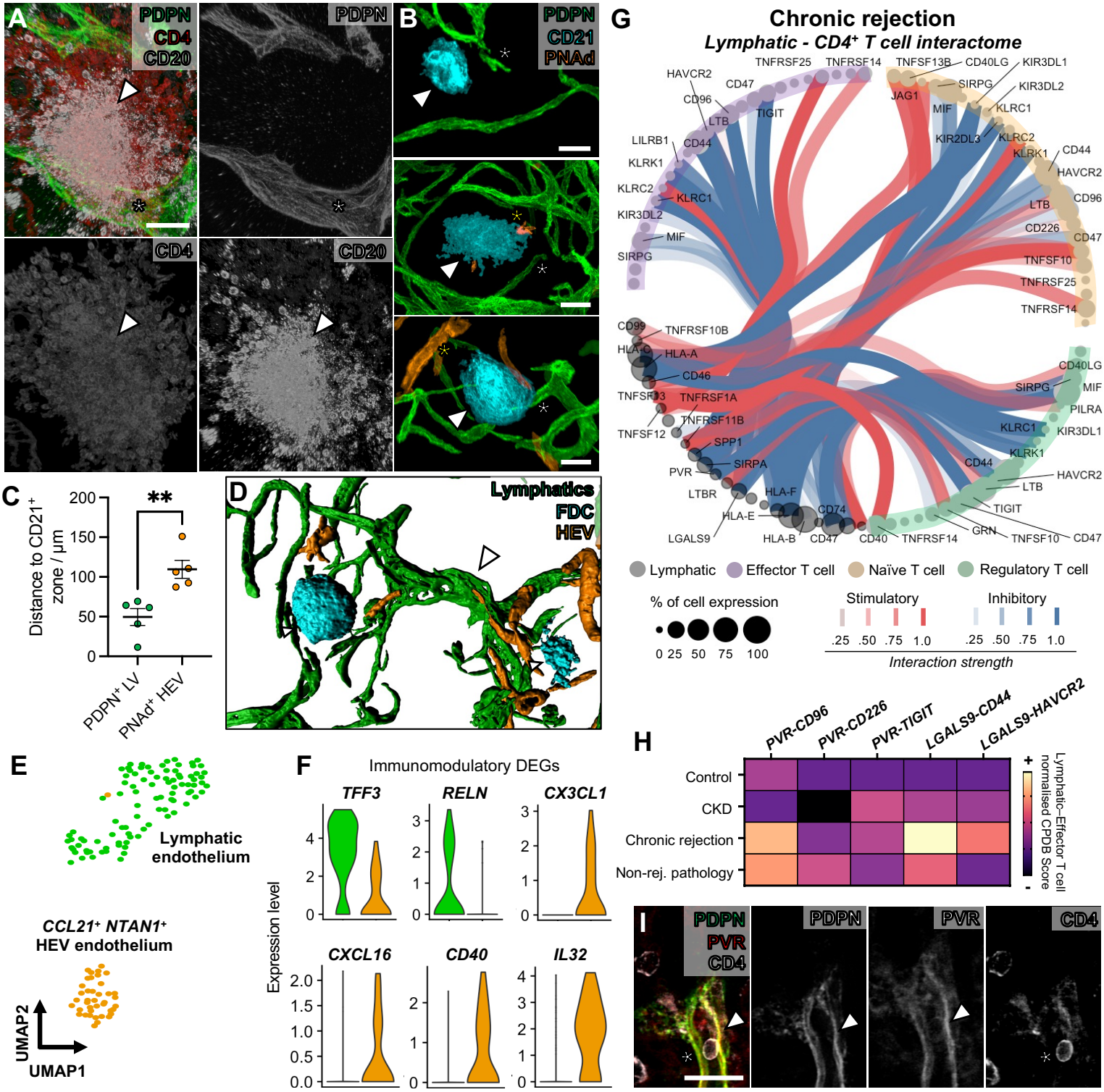
A
PDPN
CD4
CD20
B
PDPN
CD21
PNAd
C
Distance to CD21+ zone / µm
**
PDPN+ LV
PNAd+ HEV
D
Lymphatics
FDC
HEV
E
Lymphatic endothelium
CCL21+ NTAN1+ HEV endothelium
UMAP2
UMAP1
F
Immunomodulatory DEGs
TFF3
RELN
CX3CL1
CXCL16
CD40
IL32
Expression level
G
Chronic rejection
Lymphatic - CD4+ T cell interactome
Lymphatic
Effector T cell
Naïve T cell
Regulatory T cell
% of cell expression
Stimulatory
Inhibitory
Interaction strength
H
PVR-CD96
PVR-CD226
PVR-TIGIT
LGALS9-CD44
LGALS9-HAVCR2
Control
CKD
Chronic rejection
Non-rej. pathology
Lymphatic–Effector T cell normalised CPDB Score
I
PDPN
PVR
CD4

Figure 5. Interrogating the immunomodulatory molecular landscape of kidney lymphatics in alloimmunity

(**A**) Representative confocal images of PDPN$^+$ lymphatics (white asterisk), CD20$^+$ B cells and CD4$^+$ T cells in regions with evidence of lymphocyte aggregation. A tertiary lymphoid structure (TLS) is shown (white arrowhead). Representative image of 4 T cell and B cell-rich TLS taken from *n* = 2 rejecting allografts. Scale bar = 40 µm. (**B**) Representative confocal images of TLS, containing PDPN$^+$ lymphatics (white asterisk), CD21$^+$ follicular dendritic cells (white arrowhead) and peripheral lymph node addressin (PNAd)$^+$ high endothelial venules (HEV, yellow asterisk). 9 TLS were imaged across *n* = 3 rejecting allografts. Each image represents TLS at different stages, with either HEVs absent (early stage; top image), scant (mid-stage; middle image) or present (late-stage, bottom image). Scale bar = 50 µm. (**C**) 3D rendering of TLS interconnected by lymphatics, with the same molecular markers used in **B**. Such interconnections (white arrowhead) were observed between TLS in all (*n* = 3) rejecting allografts imaged. (**D**) Comparison of distance between the CD21$^+$ TLS core and lymphatic vessel (green) or HEVs (orange), with each data point representing an individual TLS imaged. Lymphatic vessels were significantly closer to the CD21$^+$ TLS core than HEVs (mean difference = 60.04, 95% CI = 24.33-95.76, p = 0.0047). **(E)** UMAP of lymphatics and blood vasculature expressing *CCL21* and *PNAd* within rejecting allografts in the scRNA-seq dataset. **(F)** Violin plots showing immunomodulatory candidates differentially expressed between lymphatic endothelium and HEV cells across rejecting allograft scRNA-seq data. Pro-reparative candidates (*TFF3, RELN*) are enriched in lymphatic endothelium whereas immune activating candidates (*CX3CL1, CXCL16, CD40, IL32*) are enriched in *CCL21*$^+$ *PNAd*$^+$ blood endothelium. **(G)** Circle plot 'interactome' of scRNA-seq data from rejecting allografts, including curated CellPhoneDB interactions derived from lymphatics and acting on different CD4$^+$ T cell subsets. Each node represents a putative ligand or receptor, with node colour as cell type. Each line represents an interaction (stimulatory interactions = red, inhibitory interactions = blue. The size of the node represents the proportion of cells expressing the ligand or receptor, and the darkness of the line represents the strength of the interaction. **(H)** Heatmaps of immune checkpoint interactions detected between lymphatics and effector CD4$^+$ T cells within the scRNAseq data across different aetiologies of disease, with colour representing the normalised CellPhoneDB score. **(I)** Imaging validation of expression of poliovirus receptor (PVR) in PDPN$^+$ lymphatics (white arrowhead) and a contacting CD4$^+$ T cell (white asterisk) from *n* = 2 rejecting allografts. Scale bar = 30 µm.

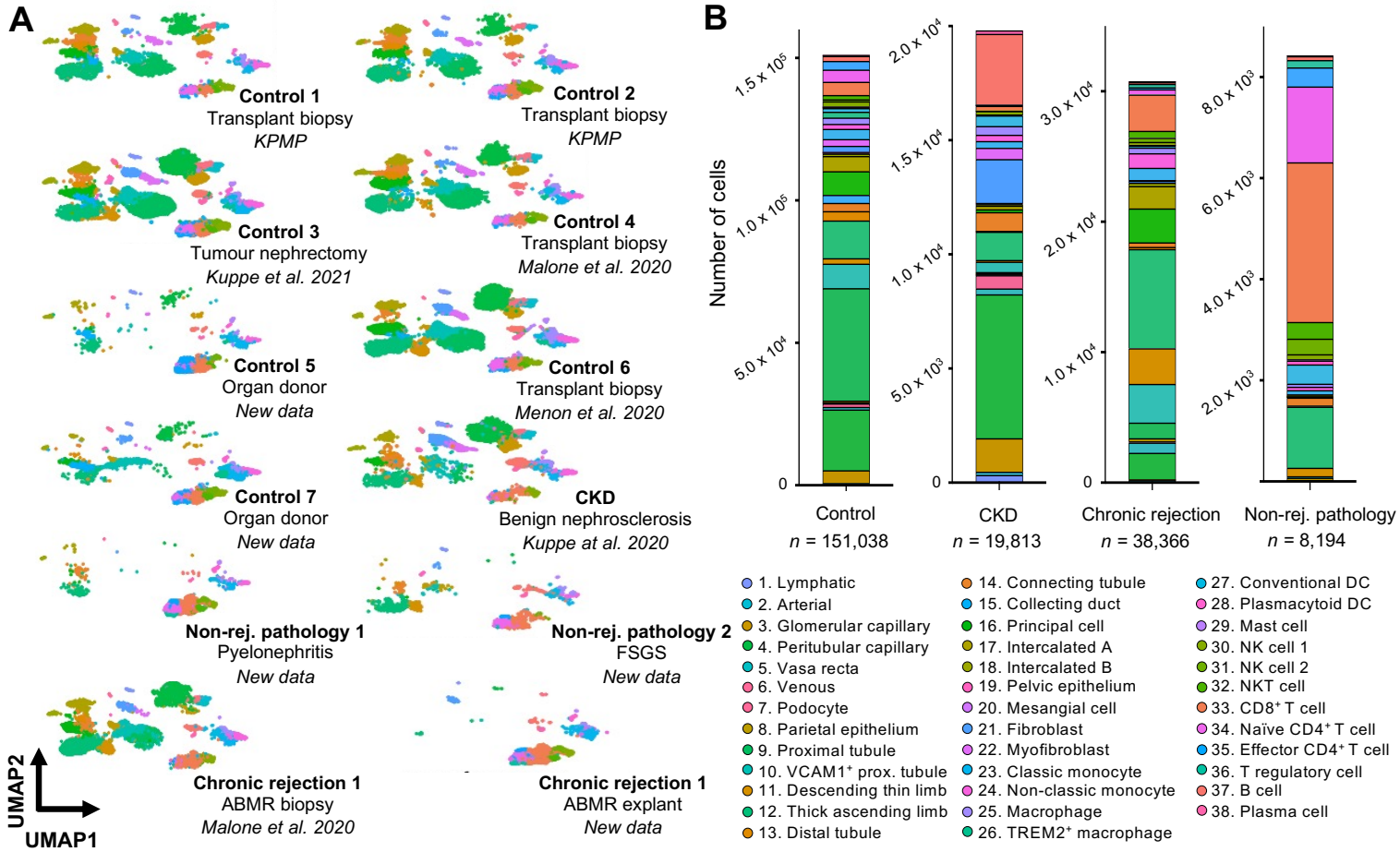
A
Control 1
Transplant biopsy
KPMP
Control 2
Transplant biopsy
KPMP
Control 3
Tumour nephrectomy
Kuppe et al. 2021
Control 4
Transplant biopsy
Malone et al. 2020
Control 5
Organ donor
New data
Control 6
Transplant biopsy
Menon et al. 2020
Control 7
Organ donor
New data
CKD
Benign nephrosclerosis
Kuppe at al. 2020
Non-rej. pathology 1
Pyelonephritis
New data
Non-rej. pathology 2
FSGS
New data
Chronic rejection 1
ABMR biopsy
Malone et al. 2020
Chronic rejection 1
ABMR explant
New data
UMAP2
UMAP1
B
Number of cells
Control
n = 151,038
CKD
n = 19,813
Chronic rejection
n = 38,366
Non-rej. pathology
n = 8,194
1. Lymphatic
2. Arterial
3. Glomerular capillary
4. Peritubular capillary
5. Vasa recta
6. Venous
7. Podocyte
8. Parietal epithelium
9. Proximal tubule
10. VCAM1+ prox. tubule
11. Descending thin limb
12. Thick ascending limb
13. Distal tubule
14. Connecting tubule
15. Collecting duct
16. Principal cell
17. Intercalated A
18. Intercalated B
19. Pelvic epithelium
20. Mesangial cell
21. Fibroblast
22. Myofibroblast
23. Classic monocyte
24. Non-classic monocyte
25. Macrophage
26. TREM2+ macrophage
27. Conventional DC
28. Plasmacytoid DC
29. Mast cell
30. NK cell 1
31. NK cell 2
32. NKT cell
33. CD8+ T cell
34. Naïve CD4+ T cell
35. Effector CD4+ T cell
36. T regulatory cell
37. B cell
38. Plasma cell

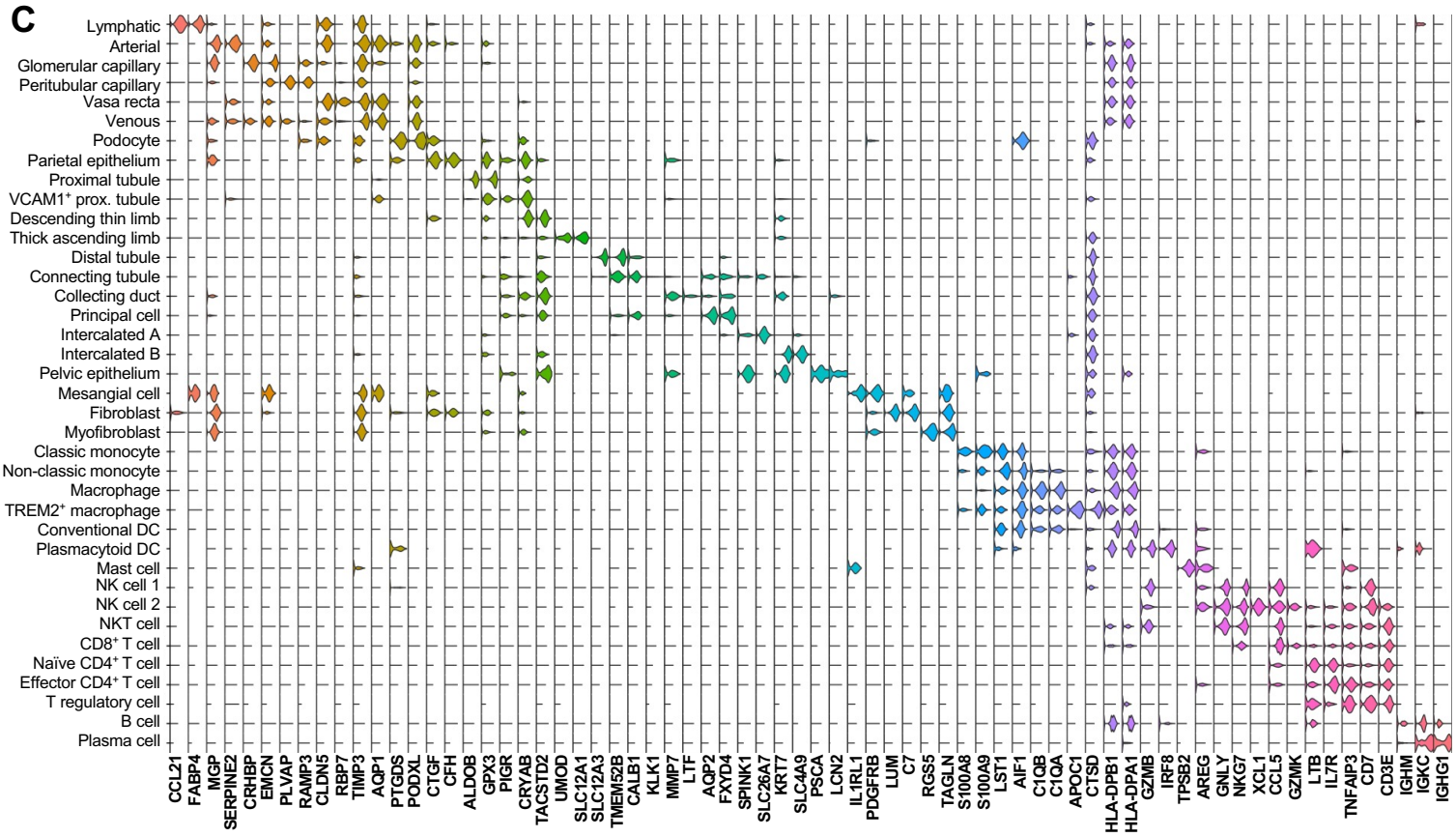
C
Lymphatic
Arterial
Glomerular capillary
Peritubular capillary
Vasa recta
Venous
Podocyte
Parietal epithelium
Proximal tubule
VCAM1+ prox. tubule
Descending thin limb
Thick ascending limb
Distal tubule
Connecting tubule
Collecting duct
Principal cell
Intercalated A
Intercalated B
Pelvic epithelium
Mesangial cell
Fibroblast
Myofibroblast
Classic monocyte
Non-classic monocyte
Macrophage
TREM2+ macrophage
Conventional DC
Plasmacytoid DC
Mast cell
NK cell 1
NK cell 2
NKT cell
CD8+ T cell
Naïve CD4+ T cell
Effector CD4+ T cell
T regulatory cell
B cell
Plasma cell
CCL21 FABP4 MGP SERPINE2 CRHBP EMCN PLVAP RAMP3 CLDN5 RBP7 TIMP3 AQP1 PTGDS PODXL CTGF CFH ALDOB GPX3 PIGR CRYAB TACSTD2 UMOD SLC12A1 SLC12A3 TMEM52B CALB1 KLK1 MMP7 LTF AQP2 FXYD4 SPINK1 SLC26A7 KRT7 SLC4A9 PSCA LCN2 IL1RL1 PDGFRB LUM C7 RGS5 TAGLN S100A8 S100A9 LST1 AIF1 C1QB C1QA APOC1 CTSD HLA-DPB1 HLA-DPA1 GZMB IRF8 TPSB2 AREG GNLY NKG7 XCL1 CCL5 GZMK LTB IL7R TNFAIP3 CD7 CD3E IGHM IGKC IGHG1

Supplementary Figure 1. Generating a human kidney single-cell transcriptomic atlas featuring health and pathologies

(**A**) Uniform manifold approximation and projection (UMAP) of the kidney cell atlas coloured by cell type and partitioned by dataset. Data sources are included under each sample label with either appropriate references, new samples or whether data was derived from the Kidney Precision Medicine Project (KPMP). Samples included non-rejection 'healthy' transplant biopsies (Control 1: 7,259 cells, Control 2: 9,785 cells, Control 4: 38,850 cells and Control 6: 22,592 cells), non-tumorous regions of tumour nephrectomies (Control 3: 58,934 cells, chronic kidney disease due to benign nephrosclerosis (CKD): 58,934 cells), declined organ donor tissues (Control 5: 3,877 cells , Control 7: 9,741 cells) and surgically explanted allografts (Non-rejection pathology 1 (chronic pyelonephritis): 6,063 cells, Non-rejection pathology 2 (focal segmental glomerulosclerosis): 2,131 cells, Chronic rejection 1: 34,067 cells, Chronic rejection 2: 4,299 cells). (**B**) Stacked bar charts representing the relative proportions of each annotated cell type across the four study groups). (**C**) Stacked violin plot showing top two differentially expressed marker genes (*y* axis) by cell type (*x* axis), calculated using Seurat FindAllMarkers function.

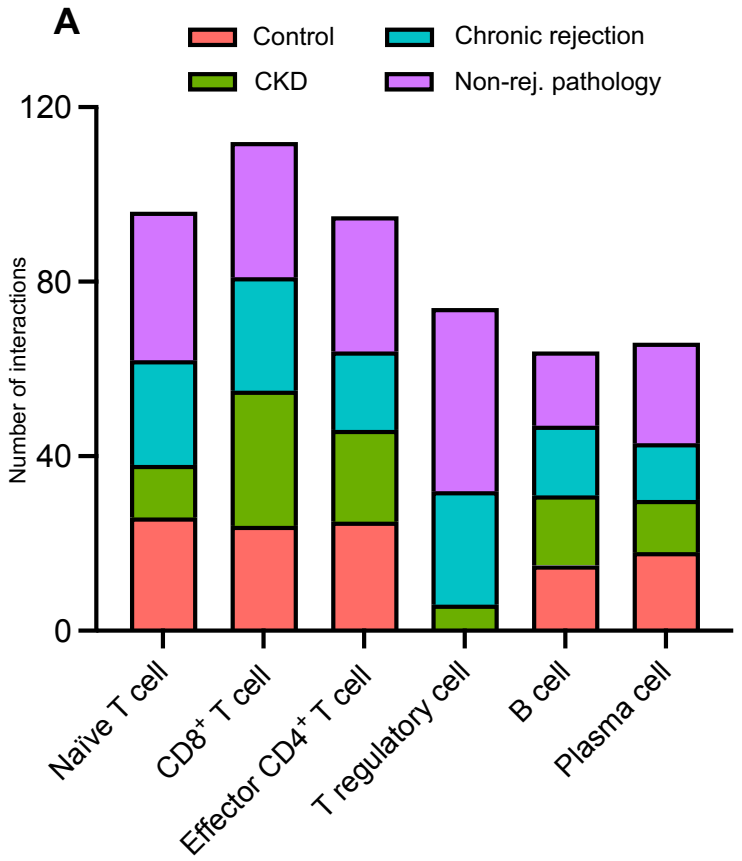
A
Control
Chronic rejection
CKD
Non-rej. pathology
Number of interactions
120
80
40
0
Naïve T cell
CD8+ T cell
Effector CD4+ T cell
T regulatory cell
B cell
Plasma cell

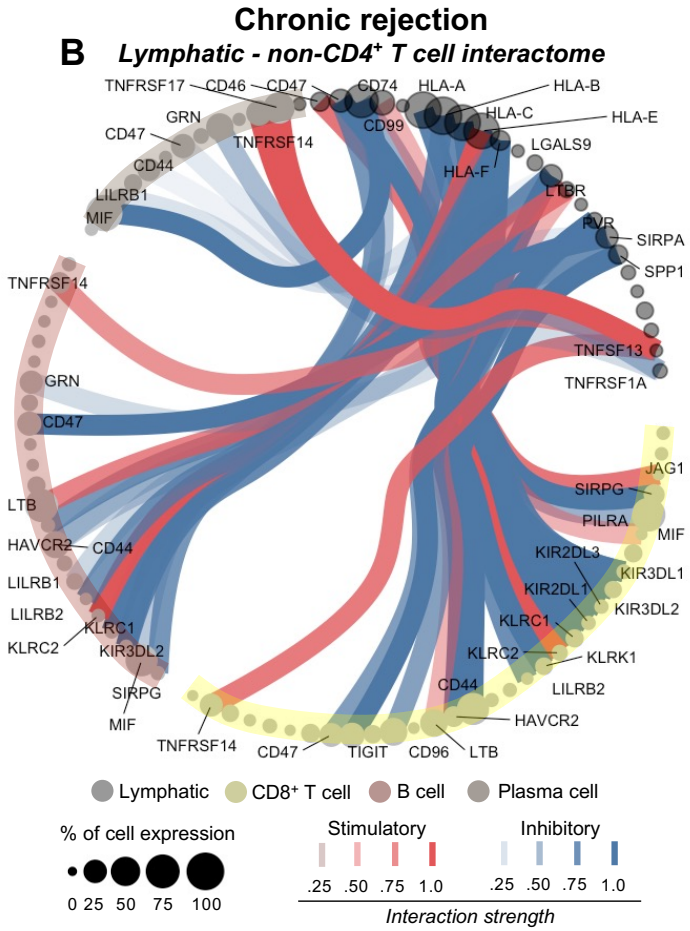
Chronic rejection
B
Lymphatic - non-CD4+ T cell interactome
Lymphatic
CD8+ T cell
B cell
Plasma cell
% of cell expression
0 25 50 75 100
Stimulatory
Inhibitory
.25 .50 .75 1.0
Interaction strength

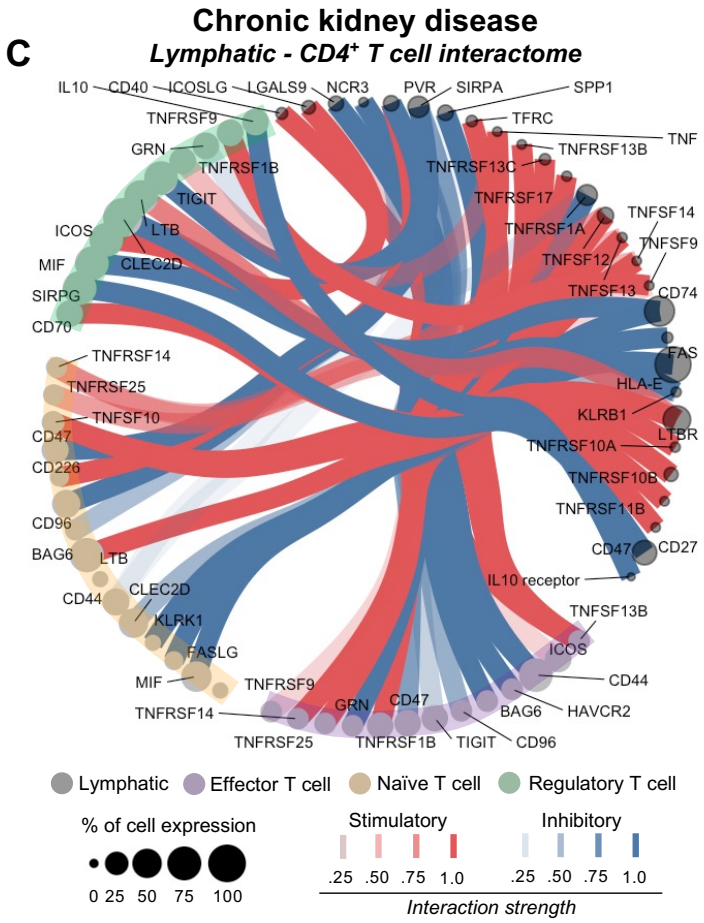
Chronic kidney disease
C
Lymphatic - CD4+ T cell interactome
Lymphatic
Effector T cell
Naïve T cell
Regulatory T cell
% of cell expression
0 25 50 75 100
Stimulatory
Inhibitory
.25 .50 .75 1.0
Interaction strength

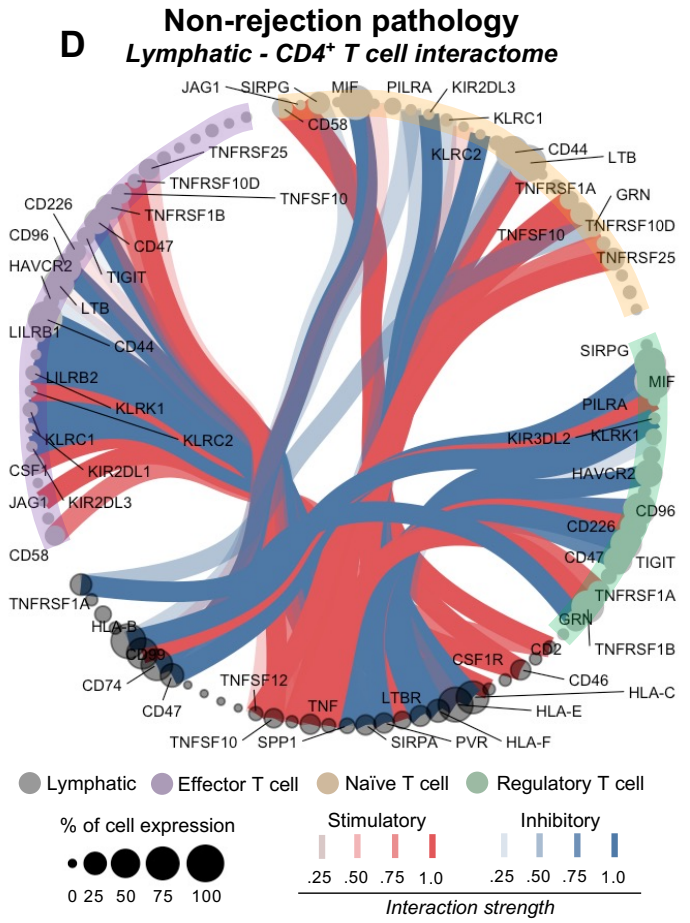
Non-rejection pathology
D
Lymphatic - CD4+ T cell interactome
Lymphatic
Effector T cell
Naïve T cell
Regulatory T cell
% of cell expression
0 25 50 75 100
Stimulatory
Inhibitory
.25 .50 .75 1.0
Interaction strength

Supplementary Figure 2. Cell-cell interactome landscape of lymphatics and adaptive immune subsets across kidney pathologies

(**A**) Bar chart showing the total number of CellPhoneDB-computed cell-cell interactions between lymphatics and adaptive immune cell subsets within single-cell RNA sequencing (scRNA-seq) data of control, chronic kidney disease (CKD), alloimmune rejection and non-alloimmune rejection tissues. (**B-D**) Circle plot of the transcriptional 'interactome', or putative cell-cell communication, between lymphatics and distinct immune cell subsets identified in the scRNA-seq dataset, computed between lymphatics and non-$CD4^+$ T cells in alloimmune rejection (**B**), lymphatics and $CD4^+$ cell subsets in CKD (**C**), and lymphatics and $CD4^+$ cell subsets in non- rejection pathology (**D**). Each node represents a putative ligand or receptor, with node colour as cell type. Each line represents an interaction, with stimulatory interactions coloured in red and inhibitory interactions coloured in blue. The size of the node represents the proportion of cells expressing the ligand or receptor, and the darkness of the line represents the strength of the CellPhoneDB interaction.

MATERIALS AND METHODS

Three-dimensional imaging and analysis of human kidney lymphatics

Acquisition, fixation and storage of human tissue for three-dimensional imaging

Human adult kidney tissue was derived from four deceased patients who had opted in for organ donation and undergone multi-organ procurement, but for whom the kidneys had ultimately been declined for implantation by recipient transplant centres. Kidneys were retrieved by a UK National Organ Retrieval Services teams. Following *in situ* flushing of the abdominal organs with University of Wisconsin (UW) solution, the kidneys were removed and stored in UW at 4°C. Consent for the use of the organs for research was obtained from the donor family by Specialist Nurses in Organ Donation before organ retrieval and were then offered for research by NHS Blood & Transplant (NHSBT) if they were found to be unsuitable for transplantation by the surgical team. Ethical approval was granted by the National Research Ethics Committee in the UK (21/WA/0388) and was approved by The Royal Free London NHS Foundation Trust-UCL Biobank Ethical Review Committee (RFL B-ERC; NC.2018.010; IRAS 208955). Kidney allograft samples were obtained from three patients at Royal Free London NHS Trust undergoing nephrectomy for graft intolerance syndrome (n = 2) and graft malignancy (n = 1). Ethical approval was covered by a prior agreement (NC.2018.007, UCL Biobank Ethical Review Committee, Royal Free London NHS Foundation Trust, B-ERC-RF). All explants were performed by the transplant surgical team. Prior to acquisition, all patients were confirmed negative for COVID-19 by means of a qPCR test. After explant, pseudo-anonymised human adult kidney tissues were incubated overnight in Belzer University of Washington Cold Storage Solution (Bridge to Life Europe, London, UK) at 4°C. Prior to fixation, human adult kidney was manually dissected into ~3mm full-thickness sub-regions containing cortex and outer medulla. These tissues were then incubated in 4% (w/v) paraformaldehyde (PFA, Sigma Aldrich), made up in 1 X phosphate buffered saline (PBS), at 4° C overnight. After fixation, all biological tissues were washed and stored in 1 X PBS with 0.02% (w/v) sodium azide to prevent contamination. Randomly

selected pieces of human adult kidney were transferred to and stored in 70% ethanol for histology

Wholemount immunofluorescence

A modified version of the SHANEL protocol (Zhao et al. 2020) was implemented for wholemount immunolabelling of kidney tissues. Unless otherwise stated, steps were performed at room temperature, and reagents purchased from Sigma Aldrich. Tissues were dehydrated in a methanol series (50, 70%) in double distilled (dd)H2O, for one hour per step, before bleaching in absolute methanol with 5% (v/v) of 30% hydrogen peroxide solution overnight at 4°C. Thereafter, tissues were rehydrated in the methanol series, followed by incubation in 1 x PBS for one hour. Overnight incubation of tissues was performed in a 0.5 M solution of acetic acid at 4°C, followed by five hours of incubation at 4°C with 4 M guanidine hydrochloride, 0.05 M sodium acetate and 2% (v/v) Triton X-100 made up in PBS. Tissues were then permeabilised with 5% (w/v) solution of 3-((3-cholamidopropyl) dimethylammonio)-1-propanesulfonate (CHAPS) made up in ddH2O overnight. Then tissues were incubated for one day in blocking solution, comprising 1 x PBS with 0.2% Triton X-100, 5% (v/v) donkey or goat serum, 5% (v/v) pooled human plasma (Biowest, Nuaillé, France) and 10% (v/v) dimethyl sulfoxide (DMSO) before incubation in antibody solution (1 x PBS with 0.2% (v/v) Tween-20, 0.1% (v/v) of a 10mg/ml heparin solution in ddH2O, 0.1% (w/v) saponin, 2.5% donkey or goat serum, 2.5% pooled human plasma with primary antibodies at the appropriate concentration at 4°C. Blocking and antibody solutions were further supplemented with 1:150 Human TruStain FcX™ Fc Receptor Blocking Solution (BioLegend, London, UK), to reduce non-specific binding. Primary antibodies were incubated for 3-4 days, before replenishing the antibody solution and re-incubation for 3-4 days. Subsequently, tissues were washed in 1 x PBS with 0.2% Tween-20 four times for 1 hour per wash, before incubation in antibody solution with secondary antibodies at 1:200 at 4°C for four days. Tissues were then washed again in 1 x

PBS with 0.2% Tween-20 four times for 1 hour each and stored until dehydration and clearing.

Primary antibodies, lectins and secondary antibodies

In order of appearance in the manuscript, the following primary antibodies or lectins were used in 1.5ml incubations at the indicated concentrations: mouse anti-PDPN monoclonal (clone: D2-40, 1:100, M3619, Aligent), rabbit anti-PROX1 polyclonal (1:200, ABN278, Merck), goat anti-LYVE1 polyclonal (1:100, AF2089, R&D Systems), fluorescein-conjugated LTL (1:50, Vector Laboratories), rabbit anti-UMOD monoclonal (clone: EPR20071, 1:100, ab207170, Abcam), fluorescein-conjugated UAE-I (1:50, Vector Laboratories), rabbit anti-LRP2 polyclonal (1:50, ab76969, Abcam), rabbit anti-CALB1 monoclonal (clone: EP3478, 1:100, ab108404, Abcam), rhodamine-conjugated DBA (1:50, Vector Laboratories), mouse anti-CDH1 monoclonal (clone: HECD-1, 1:50, ab1416, Abcam), mouse anti-PECAM1 monoclonal (clone: JC70A, 1:50, M0823, Dako), mouse anti-CD68 monoclonal (clone: KP1, 1:100, ab955, Abcam), rabbit anti-αSMA polyclonal (1:50, ab5694, Abcam), rabbit anti-HLA-DR monoclonal (clone: EPR3692, 1:100, ab92511, Abcam), rabbit anti-C4d polyclonal (1:100, 0300-0230, Bio-Rad), rabbit anti-CD4 monoclonal (clone: EPR6855, 1:100, ab133616, Abcam), goat anti-CD20 polyclonal (1:100, ab194970, Abcam), goat anti-PVR polyclonal (1:100, AF2530, R&D Systems), rabbit anti-CD21 monoclonal (clone: EPR3093, 1:200, ab75985, Abcam), rat anti-PNAd monoclonal (clone: MECA-79, 1:100, MABF2050, Sigma). All secondary antibodies were purchased from ThermoFisher Scientific, were conjugated to AlexaFluor fluorophores (488, 546, 568, 633 or 647) and were used at a concentration of 1:200 of the original secondary antibody stock. Controls for each panel involved omission of the primary antibody and including the secondary antibody only.

Solvent-based optical clearing

Tissues were dehydrated in a methanol series (50%, 70%, 100%) for 1 hour per step. BABB (benzyl alcohol and benzyl benzoate in a 1:2 ratio), was used for clearing, with all solutions

containing BABB kept in glass scintillation vials (VWR International, Lutterworth, UK). Clearing was performed in glass scintillation vials, first using BABB:methanol in a 1:1 ratio, and thereafter BABB alone, until samples equilibrated and achieved transparency.

Confocal microscopy

We took advantage of the z-depth achievable by upright confocal microscopy whilst protecting the microscope objectives. All tissues were placed between a large coverslip and cover glass, supported by a O-Ring (Polymax Ltd, Bordon, UK) made from BABB-resistant rubber, as described previously (Jafree et al. 2020). Confocal images were acquired on an LSM880 upright confocal microscope (Carl Zeiss Ltd.), with a 2.5x/numerical aperture (NA) 0.085 Pan-Neofluar Dry objective (working distance; WD = 8,800 µm) for low-resolution imaging, and 10×/NA 0.5 W-Plan Apochromat water dipping objective (working distance; WD = 3,700 µm) for high-resolution imaging. Gallium arsenide phosphide (GaAsP) internal and external detectors were used for high sensitivity. To obtain higher resolution imaging, an Airyscan setting (Huff 2015), consisting of a 32-channel (GaAsP) photomultiplier tube area detector.

Lightsheet fluorescence microscopy

3D imaging of cleared tissues was performed using a custom-built mesoscale selective plane illumination microscope (mesoSPIM) (Voigt et al. 2019). The cleared tissue was secured in a 3D-printed holder and immersed in BABB solutions inside a quartz cuvette (40 x 40 x 100 mm). Fluorescence images were acquired with an Olympus MVX-10 macroscope at 1x magnification, resulting in a voxel size of 6.55 x 6.55 x 5 μm^3. PDPN fluorescence signals were obtained using 638 nm laser excitation and 633nm long-pass optical filtering of emitted light, while autofluorescence was captured using 488 nm laser excitation and a 520/35 nm bandpass emission filter. Lightsheet illumination from both sides of the cuvette was carefully aligned after the sample was positioned at the centre of the macroscope's field of view and delivered simultaneously to capture a single *z*-stack image.

Post-acquisition image processing

All images were then exported to FIJI (NIH, Bethesda, US). Confocal image stacks were separated into individual fluorescence channels, and the Despeckle and Sharpen tools were used to reduce non-specific background fluorescence. Where maximum intensity *z*-projections or optical *z*-sections were required, scale bars were applied and images and exported as TIFF files.

Image visualisation and binarization of three-dimensional imaging data

Visualisation of confocal 3D reconstructions were performed by importing confocal images to the commercial software, Imaris (v8.2, Bitplane). The Isosurface Rendering tool in Imaris allows the extraction of surfaces based on fluorescence intensity. This was used to generate segmented images fluorescence masks to better visualise expression patterns, or to generate binarized outputs for extraction of quantitative vessel branching metrics. LSFM data was imported into Amira (v2020.2, Fisher Scientific) and the vasculature segmented using intensity thresholding and region growing using the Magic Wand tool to generate a binarized network.

Extraction of vessel branching metrics from three-dimensional imaging data

Segmented and binarized confocal and LSFM images were imported as TIFF image stacks into Amira. The Filament Editor tool was used in Amira to generate spatial statistical parameters including vessel branch number, lengths, diameter and volumes from each segmented lymphatic plexus. The resulting values were exported these as CSV files.

Spatial statistical analysis of lymphatic-lymphocyte relationships

Lymphatic 3D-skeletons were extracted from binarised confocal stacks using the BoneJ Skeletonise3d function in FIJI (Lee et al. 1994). $CD4^+$ T cell and $CD20^+$ B cell counts, centroids and areas were obtained using 3d-objectcounter with no further pre-processing

(Bolte and Cordelières 2006). The mean distance of each cell from the nearest point of the lymphatic network (*d*) was calculated using the cross-product 3D point-line distance:

$$d = \frac{|(x_0 - x_1) \times (x_0 - x_2)|}{|(x_2 - x_1)|}$$

where x_1 and x_2 are the two closest adjacent nodes from the lymphatic 3D skeleton; found by minimizing cross-nearest neighbor distances, and x_0 is the centroid of the cell of interest. To evaluate whether the cell distances were different from what would be expected by chance, within each region of interest, the $CD4^+$ T cell and $CD20^+$ B cell populations were randomly redistributed under complete spatial randomness for twenty simulations. A comparison was then made as to whether the measured mean cell-lymphatic distances fell within the 95% confidence intervals obtained through the simulations under complete spatial randomness.

Single-cell transcriptomic analysis of human kidney lymphatics

Acquisition of material for single-cell transcriptomics and generation of a human kidney cell atlas

The scRNA-seq dataset from this study consisted of previously published data and five new samples. New samples were collected under the NHSBT service (REC12/EE.0446) and included two control biopsies from kidneys donated for transplantation but deemed unsuitable for use due to renal vein thrombus or mycotic pseudoaneurysm, and three further pathological samples including one chronic rejection sample (antibody-mediated) and two samples with non-rejection pathologies (chronic pyelonephritis or focal segmental glomerulosclerosis). These tissues were processed for scRNA-seq using the 10X Genomics Chromium system as previously described (Stewart et al. 2019). Briefly, samples were manually dissected into small pieces and digested for 30 minutes at 37°C, in 25 µg/ml Liberase TM (Roche) and 50 µg/ml DNase (Sigma) in 5 ml RPMI (Gibco) using gentleMACS (Miltenyi Biotec). The suspension was passed through a 100 µm cell strainer (Falcon), washed with PBS, and enriched for live cells using a Dead Cell Removal kit (Miltenyi Biotec)

before washing with PBS. Cells were loaded according to the protocol of the Chromium single cell 3' kit (v3 Chemistry). Sequencing was performed on an Illumina Hiseq 4000. Raw reads from samples and previously published scRNA-seq data of the human kidney, including samples from non-tumorous regions of tumour nephrectomies with or without CKD (Kuppe et al. 2021), live allograft biopsies with or without antibody-mediated rejection (Malone et al. 2020), transplant biopsies from the Kidney Precision Medicine project (https://atlas.kpmp.org/repository/) were mapped and quantified using cellranger software (10X Genomics). Data then underwent quality control, normalisation, feature selection and dimension reduction using the Scanpy package in Python (Wolf et al. 2018). Integration of samples from different batches was performed using scvi-tools (Lopez et al. 2018) before semi-automated cell type annotation of clusters using CellTypist (https://www.celltypist.org). The data was then converted using seurat-disk before further analysis using the Seurat package (Hao et al. 2021) in R. Unless otherwise stated, all downstream steps were performed in Seurat.

Differential expression analysis

The *FindAllMarkers* function was used for differential expression analysis. Wilcoxon Rank Sum tests were used to assess statistically significant (adjusted p value ≤ 0.05) between average log fold change values of expression. Selected differentially expressed genes were visually represented using the *VlnPlot* function or *DoHeatMap* functions.

Gene ontology analysis

Gene ontology (GO) analysis was performed using the PANTHER tool for gene classification (Mi et al. 2021). Lists of differentially expressed genes, were exported and input into the PANTHER web tool (v16.0, http://www.pantherdb.org), using statistical overrepresentation tests to group genes using the GO biological processes complete database. Fisher's Exact tests were used to assess for statistical enrichment of genes for selected GO terms, and a false discovery rate (FDR) $p \leq 0.05$ was considered significant.

CellPhoneDB

To infer putative cell-cell interactions in single-cell RNA sequencing data, the CellPhoneDB resource (Efremova et al. 2020) was used. Using normalised count and metadata files obtained from Seurat, CellPhoneDB was called by running appropriate commands, obtained from https://github.com/Teichlab/cellphonedb, in the command line through a Python virtual environment. The *statistical_analysis* method was used to assess predicted interactions, before functions in ktPlots (https://github.com/zktuong/ktplots) were used to generate custom dot plots or circle plots.

Statistical analysis and data presentation

Sample size estimation

In prior work examining the 3D architecture of lymphatic vessels in lymphangiomatous skin biopsies, conclusions were drawn based on the evaluation of three samples within the control group (Hägerling et al. 2017), and so a minimum of three patients per group were used to draw conclusions. For scRNA-seq, the number of samples and cells to be analysed was limited by the size of the dataset. The specific number of replicates used for each experiment and the number of regions images are indicated in the figure legends,

Reproducibility

Descriptive conclusions are drawn based on a minimum of four imaging volumes of interest, each taken from samples from at least two different human kidneys. The annotated and processed Seurat object, along with the scripts used for imaging analysis and interrogation of scRNA-seq data will be made publicly available upon publication of the manuscript.

Data presentation

All confocal and brightfield images were exported and saved as TIFF files. Where brightness or contrast were adjusted, this was applied uniformly across all conditions within the same figure, and details are stated in figure legends. Graphs were generated in GraphPad PRISM

and saved as TIFF format. Visualisations from scRNA-seq analysis were performed in RStudio and PNG screenshots were taken and saved. Figures were compiled in Microsoft PowerPoint (Microsoft, Redmond, US) and saved as PDF format.

Statistics

Except for scRNA-seq analysis and lymphatic-lymphocyte spatial relationships, all remaining statistical comparisons were performed using GraphPad PRISM. A two-tailed *p* value of less than 0.05 was considered statistically significant. For continuous data, Shapiro-Wilk tests were used to assess normality of distribution and Brown-Forsythe tests were used equality of variance. Where normal distribution and equality of variances were satisfied, data is presented as mean ± standard deviation. When graphed, error bars were used to represent the standard error of the mean. Student's *t*-test was used to compare two groups and ANOVA was used to compare more than two groups, applying post-hoc Bonferroni tests to provide adjusted *p* values for multiple comparisons. Statistics for scRNA-seq analysis were performed in RStudio and are as detailed above.

REFERENCES

Adair, A., Mitchell, D.R., Kipari, T., et al. 2007. Peritubular capillary rarefaction and lymphangiogenesis in chronic allograft failure. *Transplantation* 83(12), pp. 1542–1550.
de Albuquerque, R., Komsi, E., Starskaia, I., Ullah, U. and Lahesmaa, R. 2020. The role of Interleukin-32 in Autoimmunity. *Scandinavian Journal of Immunology*, p. e13012.
Alsughayyir, J., Pettigrew, G.J. and Motallebzadeh, R. 2017. Spoiling for a Fight: B Lymphocytes As Initiator and Effector Populations within Tertiary Lymphoid Organs in Autoimmunity and Transplantation. *Frontiers in immunology* 8, p. 1639.
Anderson, A.C., Joller, N. and Kuchroo, V.K. 2016. Lag-3, Tim-3, and TIGIT: Co-inhibitory Receptors with Specialized Functions in Immune Regulation. *Immunity* 44(5), pp. 989–1004.
Banerji, S., Ni, J., Wang, S.X., et al. 1999. LYVE-1, a new homologue of the CD44 glycoprotein, is a lymph-specific receptor for hyaluronan. *The Journal of Cell Biology* 144(4), pp. 789–801.
Belle, N.M., Ji, Y., Herbine, K., et al. 2019. TFF3 interacts with LINGO2 to regulate EGFR activation for protection against colitis and gastrointestinal helminths. *Nature Communications* 10(1), p. 4408.
Bernier-Latmani, J. and Petrova, T.V. 2017. Intestinal lymphatic vasculature: structure, mechanisms and functions. *Nature Reviews. Gastroenterology & Hepatology* 14(9), pp. 510–526.
Bolte, S. and Cordelières, F.P. 2006. A guided tour into subcellular colocalization analysis in light microscopy. *Journal of Microscopy* 224(Pt 3), pp. 213–232.
Bonavita, O., Mollica Poeta, V., Setten, E., Massara, M. and Bonecchi, R. 2016. ACKR2: an atypical chemokine receptor regulating lymphatic biology. *Frontiers in immunology* 7, p. 691.
Callemeyn, J., Lamarthée, B., Koenig, A., Koshy, P., Thaunat, O. and Naesens, M. 2022. Allorecognition and the spectrum of kidney transplant rejection. *Kidney International* 101(4), pp. 692–710.
Churchill, M.J., du Bois, H., Heim, T.A., et al. 2022. Infection-induced lymphatic zippering restricts fluid transport and viral dissemination from skin. *The Journal of Experimental Medicine* 219(5).
Clayton, P.A., McDonald, S.P., Russ, G.R. and Chadban, S.J. 2019. Long-Term Outcomes after Acute Rejection in Kidney Transplant Recipients: An ANZDATA Analysis. *Journal of the American Society of Nephrology* 30(9), pp. 1697–1707.
Da Mesquita, S., Fu, Z. and Kipnis, J. 2018. The meningeal lymphatic system: A new player in neurophysiology. *Neuron* 100(2), pp. 375–388.
Da Mesquita, S., Louveau, A., Vaccari, A., et al. 2018. Functional aspects of meningeal lymphatics in ageing and Alzheimer's disease. *Nature* 560(7717), pp. 185–191.
Da Mesquita, S., Papadopoulos, Z., Dykstra, T., et al. 2021. Meningeal lymphatics affect microglia responses and anti-Aβ immunotherapy. *Nature* 593(7858), pp. 255–260.
Daniëls, L., Claas, F.H.J., Kramer, C.S.M., et al. 2020. The role of HLA-DP mismatches and donor specific HLA-DP antibodies in kidney transplantation: a case series. *Transplant Immunology*, p. 101287.
Davis, B.M., Salinas-Navarro, M., Cordeiro, M.F., Moons, L. and De Groef, L. 2017. Characterizing microglia activation: a spatial statistics approach to maximize information extraction. *Scientific Reports* 7(1), p. 1576.
Di Pilato, M., Kfuri-Rubens, R., Pruessmann, J.N., et al. 2021. CXCR6 positions cytotoxic T cells to receive critical survival signals in the tumor microenvironment. *Cell* 184(17), p. 4512–4530.e22.
Donnan, M.D., Kenig-Kozlovsky, Y. and Quaggin, S.E. 2021. The lymphatics in kidney health and disease. *Nature Reviews. Nephrology* 17(10), pp. 655–675.
Dorraji, S.E., Kanapathippillai, P., Hovd, A.-M.K., et al. 2020. Kidney Tertiary Lymphoid Structures in Lupus Nephritis Develop into Large Interconnected Networks and Resemble Lymph Nodes in Gene Signature. *The American Journal of Pathology* 190(11), pp. 2203–2225.
Drayton, D.L., Liao, S., Mounzer, R.H. and Ruddle, N.H. 2006. Lymphoid organ development: from ontogeny to neogenesis. *Nature Immunology* 7(4), pp. 344–353.
Dumas, S.J., Meta, E., Borri, M., et al. 2021. Phenotypic diversity and metabolic specialization of renal endothelial cells. *Nature Reviews. Nephrology* 17(7), pp. 441–464.
Duneton, C., Winterberg, P.D. and Ford, M.L. 2022. Activation and regulation of alloreactive T cell immunity in solid organ transplantation. *Nature Reviews. Nephrology*.
Efremova, M., Vento-Tormo, M., Teichmann, S.A. and Vento-Tormo, R. 2020. CellPhoneDB: inferring cell-cell communication from combined expression of multi-subunit ligand-receptor complexes. *Nature Protocols* 15(4), pp. 1484–1506.
Elgueta, R., Benson, M.J., de Vries, V.C., Wasiuk, A., Guo, Y. and Noelle, R.J. 2009. Molecular mechanism and function of CD40/CD40L engagement in the immune system. *Immunological Reviews* 229(1), pp. 152–172.
Garcia, J.A., Pino, P.A., Mizutani, M., et al. 2013. Regulation of adaptive immunity by the fractalkine receptor during autoimmune inflammation. *Journal of Immunology* 191(3), pp. 1063–1072.
Gkountidi, A.O., Garnier, L., Dubrot, J., et al. 2021. MHC Class II Antigen Presentation by Lymphatic Endothelial Cells in Tumors Promotes Intratumoral Regulatory T cell-Suppressive Functions. *Cancer immunology research*.
Gupta, S., Thornley, T.B., Gao, W., et al. 2012. Allograft rejection is restrained by short-lived TIM-3+PD-1+Foxp3+ Tregs. *The Journal of Clinical Investigation* 122(7), pp. 2395–2404.
Gur-Cohen, S., Yang, H., Baksh, S.C., et al. 2019. Stem cell-driven lymphatic remodeling coordinates tissue regeneration. *Science* 366(6470), pp. 1218–1225.
Hägerling, R., Drees, D., Scherzinger, A., et al. 2017. VIPAR, a quantitative approach to 3D histopathology applied to lymphatic malformations. *Journal of Clinical Investigation Insight* 2(16).

Hao, Y., Hao, S., Andersen-Nissen, E., et al. 2021. Integrated analysis of multimodal single-cell data. *Cell* 184(13), p. 3573–3587.e29.
Hariharan, S., Israni, A.K. and Danovitch, G. 2021. Long-Term Survival after Kidney Transplantation. *The New England Journal of Medicine* 385(8), pp. 729–743.
He, F.-F., Zhang, D., Chen, Q., et al. 2019. Angiopoietin-Tie signaling in kidney diseases: an updated review. *FEBS Letters* 593(19), pp. 2706–2715.
Heller, F., Lindenmeyer, M.T., Cohen, C.D., et al. 2007. The contribution of B cells to renal interstitial inflammation. *The American Journal of Pathology* 170(2), pp. 457–468.
Henri, O., Pouehe, C., Houssari, M., et al. 2016. Selective stimulation of cardiac lymphangiogenesis reduces myocardial edema and fibrosis leading to improved cardiac function following myocardial infarction. *Circulation* 133(15), p. 1484–97; discussion 1497.
Holmes, M.J., O'Morchoe, P.J. and O'Morchoe, C.C. 1977. Morphology of the intrarenal lymphatic system. Capsular and hilar communications. *The American journal of anatomy* 149(3), pp. 333–351.
Hsu, M., Laaker, C., Madrid, A., et al. 2022. Neuroinflammation creates an immune regulatory niche at the meningeal lymphatic vasculature near the cribriform plate. *Nature Immunology* 23(4), pp. 581–593.
Hu, X., Deng, Q., Ma, L., et al. 2020. Meningeal lymphatic vessels regulate brain tumor drainage and immunity. *Cell Research* 30(3), pp. 229–243.
Huang, J.L., Woolf, A.S., Kolatsi-Joannou, M., et al. 2016. Vascular endothelial growth factor C for polycystic kidney diseases. *Journal of the American Society of Nephrology* 27(1), pp. 69–77.
Huff, J. 2015. The Airyscan detector from ZEISS: confocal imaging with improved signal-to-noise ratio and super-resolution. *Nature Methods* 12(12), pp. i–ii.
Ichii, O., Hosotani, M., Masum, M.A., et al. 2022. Close Association between Altered Urine-Urothelium Barrier and Tertiary Lymphoid Structure Formation in the Renal Pelvis during Nephritis. *Journal of the American Society of Nephrology* 33(1), pp. 88–107.
Ishikawa, Y., Akasaka, Y., Kiguchi, H., et al. 2006. The human renal lymphatics under normal and pathological conditions. *Histopathology* 49(3), pp. 265–273.
Jafree, D.J. and Long, D.A. 2020. Beyond a passive conduit: implications of lymphatic biology for kidney diseases. *Journal of the American Society of Nephrology* 31(6), pp. 1178–1190.
Jafree, D.J., Long, D.A., Scambler, P.J. and Moulding, D. 2020. Tissue Clearing and Deep Imaging of the Kidney Using Confocal and Two-Photon Microscopy. *Methods in Molecular Biology* 2067, pp. 103–126.
Jafree, D.J., Moulding, D., Kolatsi-Joannou, M., et al. 2019. Spatiotemporal dynamics and heterogeneity of renal lymphatics in mammalian development and cystic kidney disease. *eLife* 8.
Jakus, Z., Gleghorn, J.P., Enis, D.R., et al. 2014. Lymphatic function is required prenatally for lung inflation at birth. *The Journal of Experimental Medicine* 211(5), pp. 815–826.
Johnson, L.A. 2021. In sickness and in health: the immunological roles of the lymphatic system. *International Journal of Molecular Sciences* 22(9).
Jourde-Chiche, N., Fakhouri, F., Dou, L., et al. 2019. Endothelium structure and function in kidney health and disease. *Nature Reviews. Nephrology* 15(2), pp. 87–108.
Kahn, H.J., Bailey, D. and Marks, A. 2002. Monoclonal antibody D2-40, a new marker of lymphatic endothelium, reacts with Kaposi's sarcoma and a subset of angiosarcomas. *Modern Pathology* 15(4), pp. 434–440.
Kenig-Kozlovsky, Y., Scott, R.P., Onay, T., et al. 2018. Ascending Vasa Recta Are Angiopoietin/Tie2-Dependent Lymphatic-Like Vessels. *Journal of the American Society of Nephrology* 29(4), pp. 1097–1107.
Kerjaschki, D., Huttary, N., Raab, I., et al. 2006. Lymphatic endothelial progenitor cells contribute to de novo lymphangiogenesis in human renal transplants. *Nature Medicine* 12(2), pp. 230–234.
Kerjaschki, D., Regele, H.M., Moosberger, I., et al. 2004. Lymphatic neoangiogenesis in human kidney transplants is associated with immunologically active lymphocytic infiltrates. *Journal of the American Society of Nephrology* 15(3), pp. 603–612.
Kim, Y.-M., Kim, W.-Y., Nam, S.A., et al. 2015. Role of Prox1 in the Transforming Ascending Thin Limb of Henle's Loop during Mouse Kidney Development. *Plos One* 10(5), p. e0127429.
Klotz, L., Norman, S., Vieira, J.M., et al. 2015. Cardiac lymphatics are heterogeneous in origin and respond to injury. *Nature* 522(7554), pp. 62–67.
Kosmoliaptsis, V., Gjorgjimajkoska, O., Sharples, L.D., et al. 2014. Impact of donor mismatches at individual HLA-A, -B, -C, -DR, and -DQ loci on the development of HLA-specific antibodies in patients listed for repeat renal transplantation. *Kidney International* 86(5), pp. 1039–1048.
Kuppe, C., Ibrahim, M.M., Kranz, J., et al. 2021. Decoding myofibroblast origins in human kidney fibrosis. *Nature* 589(7841), pp. 281–286.
Lee, H.-W., Qin, Y.-X., Kim, Y.-M., et al. 2011. Expression of lymphatic endothelium-specific hyaluronan receptor LYVE-1 in the developing mouse kidney. *Cell and Tissue Research* 343(2), pp. 429–444.
Lee, K.M., McKimmie, C.S., Gilchrist, D.S., et al. 2011. D6 facilitates cellular migration and fluid flow to lymph nodes by suppressing lymphatic congestion. *Blood* 118(23), pp. 6220–6229.
Lee, T.C., Kashyap, R.L. and Chu, C.N. 1994. Building Skeleton Models via 3-D Medial Surface Axis Thinning Algorithms. *CVGIP: Graphical Models and Image Processing* 56(6), pp. 462–478.
Lee, Y., Chin, R.K., Christiansen, P., et al. 2006. Recruitment and activation of naive T cells in the islets by lymphotoxin beta receptor-dependent tertiary lymphoid structure. *Immunity* 25(3), pp. 499–509.
Lee, Y.H., Sato, Y., Saito, Mitsuru, et al. 2022. Advanced Tertiary Lymphoid Tissues in Protocol Biopsies are Associated with Progressive Graft Dysfunction in Kidney Transplant Recipients. *Journal of the American Society of Nephrology* 33(1), pp. 186–200.

Lin, J., Chen, Y., Zhu, H., et al. 2021. Lymphatic reconstruction in kidney allograft aggravates chronic rejection by promoting alloantigen presentation. *Frontiers in immunology* 12, p. 796260.
Liu, H., Hiremath, C., Patterson, Q., et al. 2021. Heterozygous Mutation of Vegfr3 Reduces Renal Lymphatics without Renal Dysfunction. *Journal of the American Society of Nephrology*.
Liu, X., De la Cruz, E., Gu, X., et al. 2020. Lymphoangiocrine signals promote cardiac growth and repair. *Nature* 588(7839), pp. 705–711.
Lopez, R., Regier, J., Cole, M.B., Jordan, M.I. and Yosef, N. 2018. Deep generative modeling for single-cell transcriptomics. *Nature Methods* 15(12), pp. 1053–1058.
Loupy, A. and Lefaucheur, C. 2018. Antibody-Mediated Rejection of Solid-Organ Allografts. *The New England Journal of Medicine* 379(12), pp. 1150–1160.
Loupy, A., Mengel, M. and Haas, M. 2022. Thirty years of the International Banff Classification for Allograft Pathology: the past, present, and future of kidney transplant diagnostics. *Kidney International* 101(4), pp. 678–691.
Luther, S.A., Bidgol, A., Hargreaves, D.C., et al. 2002. Differing activities of homeostatic chemokines CCL19, CCL21, and CXCL12 in lymphocyte and dendritic cell recruitment and lymphoid neogenesis. *Journal of Immunology* 169(1), pp. 424–433.
Malone, A.F., Wu, H., Fronick, C., Fulton, R., Gaut, J.P. and Humphreys, B.D. 2020. Harnessing expressed single nucleotide variation and single cell RNA sequencing to define immune cell chimerism in the rejecting kidney transplant. *Journal of the American Society of Nephrology* 31(9), pp. 1977–1986.
Marshall, J.L., Noel, T., Wang, Q.S., et al. 2022. High-resolution Slide-seqV2 spatial transcriptomics enables discovery of disease-specific cell neighborhoods and pathways. *iScience* 25(4), p. 104097.
Meylan, M., Petitprez, F., Becht, E., et al. 2022. Tertiary lymphoid structures generate and propagate anti-tumor antibody-producing plasma cells in renal cell cancer. *Immunity* 55(3), p. 527–541.e5.
Mi, H., Ebert, D., Muruganujan, A., et al. 2021. PANTHER version 16: a revised family classification, tree-based classification tool, enhancer regions and extensive API. *Nucleic Acids Research* 49(D1), pp. D394–D403.
Motallebzadeh, R., Rehakova, S., Conlon, T.M., et al. 2012. Blocking lymphotoxin signaling abrogates the development of ectopic lymphoid tissue within cardiac allografts and inhibits effector antibody responses. *The FASEB Journal* 26(1), pp. 51–62.
Muczynski, K.A., Cotner, T. and Anderson, S.K. 2001. Unusual expression of human lymphocyte antigen class II in normal renal microvascular endothelium. *Kidney International* 59(2), pp. 488–497.
Muczynski, K.A., Ekle, D.M., Coder, D.M. and Anderson, S.K. 2003. Normal human kidney HLA-DR-expressing renal microvascular endothelial cells: characterization, isolation, and regulation of MHC class II expression. *Journal of the American Society of Nephrology* 14(5), pp. 1336–1348.
Oliver, G., Kipnis, J., Randolph, G.J. and Harvey, N.L. 2020. The lymphatic vasculature in the 21st century: novel functional roles in homeostasis and disease. *Cell* 182(2), pp. 270–296.
Ouimet, M., Barrett, T.J. and Fisher, E.A. 2019. HDL and reverse cholesterol transport. *Circulation Research* 124(10), pp. 1505–1518.
Palin, N.K., Savikko, J. and Koskinen, P.K. 2013. Sirolimus inhibits lymphangiogenesis in rat renal allografts, a novel mechanism to prevent chronic kidney allograft injury. *Transplant International* 26(2), pp. 195–205.
Paulsen, F.P., Woon, C.-W., Varoga, D., et al. 2008. Intestinal trefoil factor/TFF3 promotes re-epithelialization of corneal wounds. *The Journal of Biological Chemistry* 283(19), pp. 13418–13427.
Pedersen, M.S., Müller, M., Rülicke, T., et al. 2020. Lymphangiogenesis in a mouse model of renal transplant rejection extends life span of the recipients. *Kidney International* 97(1), pp. 89–94.
Peña-Jimenez, D., Fontenete, S., Megias, D., et al. 2019. Lymphatic vessels interact dynamically with the hair follicle stem cell niche during skin regeneration in vivo. *The EMBO Journal* 38(19), p. e101688.
Petrova, T.V. and Koh, G.Y. 2020. Biological functions of lymphatic vessels. *Science* 369(6500).
Petrova, T.V. and Koh, G.Y. 2018. Organ-specific lymphatic vasculature: From development to pathophysiology. *The Journal of Experimental Medicine* 215(1), pp. 35–49.
Reed, H.O., Wang, L., Sonett, J., et al. 2019. Lymphatic impairment leads to pulmonary tertiary lymphoid organ formation and alveolar damage. *The Journal of Clinical Investigation* 129(6), pp. 2514–2526.
Robson, K.J. and Kitching, A.R. 2020. Tertiary lymphoid tissue in kidneys: understanding local immunity and inflammation. *Kidney International* 98(2), pp. 280–283.
Rodas, L., Barnadas, E., Pereira, A., et al. 2022. The density of renal lymphatics correlates with clinical outcomes in IgA nephropathy. *Kidney international reports*.
Ruddle, N.H. 2016. High endothelial venules and lymphatic vessels in tertiary lymphoid organs: characteristics, functions, and regulation. *Frontiers in immunology* 7, p. 491.
Russell, P.S., Hong, J., Windsor, J.A., Itkin, M. and Phillips, A.R.J. 2019. Renal lymphatics: anatomy, physiology, and clinical implications. *Frontiers in physiology* 10, p. 251.
Sakamoto, I., Ito, Y., Mizuno, M., et al. 2009. Lymphatic vessels develop during tubulointerstitial fibrosis. *Kidney International* 75(8), pp. 828–838.
Sato, Y., Boor, P., Fukuma, S., et al. 2020. Developmental stages of tertiary lymphoid tissue reflect local injury and inflammation in mouse and human kidneys. *Kidney International* 98(2), pp. 448–463.
Sato, Y., Tamura, M. and Yanagita, M. 2021. Tertiary lymphoid tissues: a regional hub for kidney inflammation. *Nephrology, Dialysis, Transplantation*.
Schröder, A.E., Greiner, A., Seyfert, C. and Berek, C. 1996. Differentiation of B cells in the nonlymphoid tissue of the synovial membrane of patients with rheumatoid arthritis. *Proceedings of the National Academy of Sciences of the United States of America* 93(1), pp. 221–225.

Shi, M., Ma, L. and Fu, P. 2020. Role of fatty acid binding protein 4 (FABP4) in kidney disease. *Current Medicinal Chemistry* 27(22), pp. 3657–3664.
Song, E., Mao, T., Dong, H., et al. 2020. VEGF-C-driven lymphatic drainage enables immunosurveillance of brain tumours. *Nature* 577(7792), pp. 689–694.
Steele, M.M., Dryg, I.D., Murugan, D., et al. 2022. T cell Egress via Lymphatic Vessels Limits the Intratumoral T cell Repertoire in Melanoma. *BioRxiv*.
Steele, M.M. and Lund, A.W. 2021. Afferent lymphatic transport and peripheral tissue immunity. *Journal of Immunology* 206(2), pp. 264–272.
Stewart, B.J., Ferdinand, J.R., Young, M.D., et al. 2019. Spatiotemporal immune zonation of the human kidney. *Science* 365(6460), pp. 1461–1466.
Stritt, S., Koltowska, K. and Mäkinen, T. 2021. Homeostatic maintenance of the lymphatic vasculature. *Trends in Molecular Medicine* 27(10), pp. 955–970.
Stuht, S., Gwinner, W., Franz, I., et al. 2007. Lymphatic neoangiogenesis in human renal allografts: results from sequential protocol biopsies. *American Journal of Transplantation* 7(2), pp. 377–384.
Sun, H., Hartigan, C.R., Chen, C.-W., et al. 2021. TIGIT regulates apoptosis of risky memory T cell subsets implicated in belatacept-resistant rejection. *American Journal of Transplantation*.
Szőke, D., Kovács, G., Kemecsei, É., et al. 2021. Nucleoside-modified VEGFC mRNA induces organ-specific lymphatic growth and reverses experimental lymphedema. *Nature Communications* 12(1), p. 3460.
Talsma, D.T., Katta, K., Boersema, M., et al. 2017. Increased migration of antigen presenting cells to newly-formed lymphatic vessels in transplanted kidneys by glycol-split heparin. *Plos One* 12(6), p. e0180206.
Tanaka, K., Sugiyama, H., Yamanari, T., et al. 2018. Renal expression of trefoil factor 3 mRNA in association with tubulointerstitial fibrosis in IgA nephropathy. *Nephrology* 23(9), pp. 855–862.
Thaunat, O., Kerjaschki, D. and Nicoletti, A. 2006. Is defective lymphatic drainage a trigger for lymphoid neogenesis? *Trends in Immunology* 27(10), pp. 441–445.
Tsuchimoto, A., Nakano, T., Hasegawa, S., et al. 2017. The potential role of perivascular lymphatic vessels in preservation of kidney allograft function. *Clinical and experimental nephrology* 21(4), pp. 721–731.
Vass, D.G., Hughes, J. and Marson, L.P. 2009. Restorative and rejection-associated lymphangiogenesis after renal transplantation: friend or foe? *Transplantation* 88(11), pp. 1237–1239.
Vass, D.G., Shrestha, B., Haylor, J., Hughes, J. and Marson, L. 2012. Inflammatory lymphangiogenesis in a rat transplant model of interstitial fibrosis and tubular atrophy. *Transplant International* 25(7), pp. 792–800.
Vieira, J.M., Norman, S., Villa Del Campo, C., et al. 2018. The cardiac lymphatic system stimulates resolution of inflammation following myocardial infarction. *The Journal of Clinical Investigation* 128(8), pp. 3402–3412.
Voigt, F.F., Kirschenbaum, D., Platonova, E., et al. 2019. The mesoSPIM initiative: open-source light-sheet microscopes for imaging cleared tissue. *Nature Methods* 16(11), pp. 1105–1108.
Wang, Y., Jin, Y., Mäe, M.A., et al. 2017. Smooth muscle cell recruitment to lymphatic vessels requires PDGFB and impacts vessel size but not identity. *Development* 144(19), pp. 3590–3601.
Wigle, J.T. and Oliver, G. 1999. Prox1 function is required for the development of the murine lymphatic system. *Cell* 98(6), pp. 769–778.
Wolf, F.A., Angerer, P. and Theis, F.J. 2018. SCANPY: large-scale single-cell gene expression data analysis. *Genome Biology* 19(1), p. 15.
Wong, B.W. 2020. Lymphatic vessels in solid organ transplantation and immunobiology. *American Journal of Transplantation* 20(8), pp. 1992–2000.
Wong, B.W., Zecchin, A., García-Caballero, M. and Carmeliet, P. 2018. Emerging Concepts in Organ-Specific Lymphatic Vessels and Metabolic Regulation of Lymphatic Development. *Developmental Cell* 45(3), pp. 289–301.
Yoon, S.-Y., Dieterich, L.C., Karaman, S., et al. 2019. An important role of cutaneous lymphatic vessels in coordinating and promoting anagen hair follicle growth. *Plos One* 14(7), p. e0220341.
Yoon, Y.-S., Murayama, T., Gravereaux, E., et al. 2003. VEGF-C gene therapy augments postnatal lymphangiogenesis and ameliorates secondary lymphedema. *The Journal of Clinical Investigation* 111(5), pp. 717–725.
Zhao, S., Todorov, M.I., Cai, R., et al. 2020. Cellular and molecular probing of intact human organs. *Cell* 180(4), p. 796–812.e19.